

Near-solidus Melting of the Shallow Upper Mantle: Partial Melting Experiments on Depleted Peridotite

LAURA E. WASYLENKI*, MICHAEL B. BAKER, ADAM J. R. KENT
AND EDWARD M. STOLPER

DIVISION OF GEOLOGICAL AND PLANETARY SCIENCES, CALIFORNIA INSTITUTE OF TECHNOLOGY,
MAIL CODE 170-25, PASADENA, CA 91125, USA

RECEIVED SEPTEMBER 18, 2001; ACCEPTED FEBRUARY 5, 2003

We present the results of melting experiments on a moderately depleted peridotite composition (DMM1) at 10 kbar and 1250–1390°C. Specially designed experiments demonstrate that liquids extracted into aggregates of vitreous carbon spheres maintained chemical contact with the bulk charge down to melt fractions of ~0.02–0.04 and approached equilibrium closely. With increasing melt fraction, SiO₂, FeO, and MgO contents of the partial melts increase, Al₂O₃ and Na₂O contents decrease, and CaO contents first increase up to clinopyroxene-out at a melt fraction of 0.09–0.10, then decrease with further melting. A linear fit to melt fraction vs temperature data for lherzolite-bearing experiments yields a solidus of 1272 ± 11°C. The melting reaction is 0.56 orthopyroxene + 0.72 clinopyroxene + 0.04 spinel = 0.34 olivine + 1 liquid. Above clinopyroxene-out, the reaction is 1.24 orthopyroxene = 0.24 olivine + 1 liquid. Near the solidus, DMM1 glass compositions have lower SiO₂, TiO₂, Na₂O, and K₂O contents, higher FeO*, MgO, and CaO contents, and higher CaO/Al₂O₃ ratios compared with glasses from low-degree melting of fertile peridotite compositions. Recent computational models predict partial melting trends generally parallel to our experimental results. We present a parameterization of 10 kbar peridotite solidus temperatures suggesting that K₂O and P₂O₅ have greater effects on solidus depression than Na₂O, consistent with theoretical expectations. Our parameterization also suggests that abyssal peridotites have 10 kbar solidi of ~1278–1295°C.*

KEY WORDS: *depleted; experimental petrology; mantle melting; near-solidus; peridotite*

*Corresponding author. Present address: Department of Geological Sciences, 4044 Derring Hall, Virginia Polytechnic Institute and State University, Blacksburg, VA 24061, USA. Telephone: 540-231-2403. Fax: 540-231-3386. E-mail: lew@vt.edu

†Present address: Department of Geosciences, Wilkinson Hall, Oregon State University, Corvallis, OR 97331, USA.

INTRODUCTION

It is widely accepted that parental magmas of mid-ocean ridge basalts (MORBs) represent a mixture of liquids produced by pressure-release melting over a range of depths in the Earth's upper mantle (e.g. McKenzie, 1984; McKenzie & Bickle, 1988; Langmuir *et al.*, 1992). Experimental and theoretical studies indicate that small amounts of melt (<2%) are interconnected in olivine-dominated, partially molten systems (e.g. Waff & Bulau, 1979; von Bagen & Waff, 1986; Daines & Richter, 1988) and that such low degrees of melt can move relative to the residual solid phases (McKenzie, 1985, 1989; Stevenson & Scott, 1991). The extremely depleted rare earth element patterns observed in residual clinopyroxenes from dredged abyssal peridotites have been used as evidence of this mobility and that melt production beneath mid-ocean ridges can approach the limit of fractional melting (Johnson *et al.*, 1990; Johnson & Dick, 1992; Salters & Dick, 2002). Correlations between the major element compositions of spinels and the concentrations of moderately incompatible trace elements in clinopyroxenes from abyssal peridotites also suggest that these peridotites experienced near-fractional melting (Hellebrand *et al.*, 2000). Finally, melt inclusions with variably depleted trace element concentrations relative to average MORB (e.g. Sobolev & Shimizu, 1993; Sobolev, 1996; Shimizu, 1998) suggest that erupted MORB magmas contain a component of liquid produced by melting of depleted peridotite. Taken together, these lines of evidence suggest that

partial melts can be extracted from the mantle beneath mid-ocean ridges at low melt fractions and that at least some components of MORBs were produced by melting of depleted sources with low concentrations of incompatible major, minor, and trace elements relative to the fertile MORB source.

Most high-pressure experimental studies of peridotite melting have focused on fertile mantle compositions, and these studies have provided information on melt compositions over a wide range of pressures and temperatures (e.g. Jaques & Green, 1980; Takahashi, 1986; Hirose & Kushiro, 1993; Baker & Stolper, 1994; Baker *et al.*, 1995; Kushiro, 1996; Robinson *et al.*, 1998; Walter, 1998). In addition, Pickering-Witter & Johnston (2000) and Schwab & Johnston (2001) explored the effects of pyroxene and spinel abundances and pyroxene compositions on liquid compositions, melt productivities, and melting reactions at 10 kbar, and, by varying the orthopyroxene/clinopyroxene ratios in their starting materials, they were able to work on bulk compositions spanning wide ranges of MgO, Al₂O₃, CaO, and Na₂O contents.

In a synthesis of available experimental data, Hirschmann *et al.* (1998a) showed the important role that alkalis play in controlling the compositions of olivine + orthopyroxene ± clinopyroxene-saturated melts of peridotite. Likewise, the broadly inverse correlation between total alkali contents of peridotites and their solidus temperatures (Herzberg *et al.*, 2000; Hirschmann, 2000) suggests that, at a given pressure, depleted peridotites will begin to melt at higher temperatures than fertile peridotites. Because peridotites in the shallowest part of the melting zone beneath mid-ocean ridges are expected to have been depleted in incompatible major and minor elements (and especially alkalis) by prior melting, the expectation is that such peridotites would melt to a lower degree and produce different liquids compared with melting of fertile peridotite under similar conditions.

In this paper we present the results of melting experiments on a moderately depleted peridotite composition (DMM1) at 10 kbar and 1250–1390°C; these results complement the large amount of available data on more fertile peridotite compositions. We used a variant of the diamond aggregate melt-extraction technique developed by Johnson & Kushiro (1992), Hirose & Kushiro (1993), and Baker & Stolper (1994) to study near-solidus experimental glasses unmodified by quench crystal growth. In the experiments described here, the aggregate comprised vitreous carbon spheres or fragments (Wasylenki *et al.*, 1996; Pickering-Witter & Johnston, 2000; Schwab & Johnston, 2001). A potential problem associated with the diamond aggregate technique in low melt fraction experiments is that pressure is initially low within the void spaces of the

aggregate until the layer is completely filled with melt (Baker *et al.*, 1996), possibly leading to the segregation of liquid that is far from equilibrium with the peridotite at the actual pressure of the experiment. The motivation for replacing the porous diamond aggregate used in our previous studies (Baker & Stolper, 1994; Baker *et al.*, 1995) with vitreous carbon spheres is that, although vitreous carbon is strong enough to support open pore space at the start of an experiment, it is much less stiff than diamond (Noda *et al.*, 1969; Sawa & Tanaka, 2002), so this open space collapses more quickly. Another advantage is that vitreous carbon is readily polished at the end of an experiment, allowing small pools of melt to be imaged and analyzed *in situ* with ease (e.g. Pickering-Witter & Johnston, 2000; Schwab & Johnston, 2001). In addition to modifying the melt-extraction technique in this way, we have addressed the controversy surrounding this technique (see Baker *et al.*, 1996; Falloon *et al.*, 1996, 1997, 1999; Wasylenki *et al.*, 1996; Pickering-Witter & Johnston, 2000) with special experiments that demonstrate the reliability and close approach to equilibrium of melt-extraction experiments.

Following the presentation of the experimental results, we consider the effects of bulk composition on 10 kbar melting reaction coefficients and on melt productivity, and we compare our experimental glass compositions for the depleted peridotite DMM1 with those produced by melting more fertile peridotite compositions at the same pressure. We also compare our experimental glass compositions with liquid compositions calculated for the DMM1 composition using four peridotite melting models. Finally, by combining our experimentally determined 10 kbar solidus temperature with solidus determinations on other peridotite compositions, we develop a simple expression for predicting the solidus temperature at 10 kbar as a function of bulk composition.

EXPERIMENTAL AND ANALYTICAL TECHNIQUES

Starting materials

Starting materials for this study were prepared by mixing mineral separates (olivine, *ol*; orthopyroxene, *opx*; clinopyroxene, *cpx*; spinel, *sp*) from a Kilbourne Hole spinel lherzolite nodule (KBH), olivine from a Hawaiian dunite nodule (H1801i), and synthetic diopside (CaMgSi₂O₆). Electron microprobe analyses of the natural minerals are reported in Table 1. The crystallinity of the synthetic diopside was verified by X-ray diffraction, and the composition reported in Table 1 is that of stoichiometric diopside. The natural minerals were hand-picked from disaggregated

Table 1: Compositions of starting materials and bulk composition of DMM1

	SiO ₂	TiO ₂	Al ₂ O ₃	Cr ₂ O ₃	FeO*	MnO	MgO	CaO	Na ₂ O	K ₂ O	NiO	mg-no.
KBH ol(10) ¹	40.76(16)	—	0.01(1)	0.01(1)	9.34(10)	0.12(2)	49.49(21)	0.07(1)	—	—	0.39(2)	90.4(5)
H1801i ol(14) ²	40.40(17)	—	0.01(1)	0.02(2)	12.07(71)	0.17(2)	47.55(55)	0.16(2)	—	—	0.39(4)	87.5(15)
KBH opx(8)	54.99(22)	0.10(2)	4.76(15)	0.50(4)	5.98(6)	0.13(2)	32.79(14)	0.86(2)	0.12(1)	—	0.11(2)	90.7(5)
KBH cpx(15)	51.99(21)	0.41(5)	6.56(11)	1.00(5)	2.81(4)	0.09(2)	15.24(10)	19.89(11)	1.58(3)	—	0.04(2)	90.6(8)
Diopside ³	55.49	—	—	—	—	—	18.61	25.89	—	—	—	—
KBH sp(11)	0.11(2)	0.11(2)	54.91(27)	12.96(20)	10.54(11)	0.10(2)	20.95(10)	—	—	—	0.37(2)	78.0(5)
DMM1 ⁴	44.91(11)	0.04(1)	2.38(5)	0.39(1)	8.34(15)	0.13(1)	41.59(15)	2.14(2)	0.055(3)	0.006(2)	0.28(1)	89.9(5)
FB	46.59(8)	0.41(2)	13.78(5)	0.32(1)	12.07(10)	0.10(2)	11.95(3)	12.06(3)	1.39(2)	—	0.01(1)	63.8(3)
GBR ⁵	77.6	0.07	12.9	—	0.4	0.04	0.05	0.5	4.2	4.2	—	18.2

ol, olivine; opx, orthopyroxene; cpx, clinopyroxene; sp, spinel; DMM1, bulk composition used in this study; FB, ferrobasalt; GBR, Glass Buttes rhyolite. FeO*, all Fe as FeO; mg-no. = 100MgO/(MgO + FeO*) on a molar basis.

¹Minerals designated by KBH were separated from a Kilbourne Hole nodule; number of electron microprobe analyses in parentheses, each analysis on a separate grain. Numbers in parentheses adjacent to each oxide value are one sample standard deviation in terms of the least units cited, e.g. 40.76(16) represents 40.76 ± 0.16 . Dashes indicate that the element was not analyzed or was below the detection limit of the microprobe.

²Olivine separated from a dunite nodule collected from the Hualalai 1801 flow.

³Synthetic crystalline diopside; crystallinity verified by X-ray diffraction. Listed composition is for end-member diopside.

⁴Bulk composition (with the exception of K₂O and P₂O₅) calculated from constituent mineral compositions and mineral proportions given in text. Mean bulk K₂O content calculated from liquid K₂O contents in runs 22, 12, 27C, 28C, 33C, and 42C; phase proportions; and K₂O partition coefficients from Halliday *et al.* (1995). Mean bulk P₂O₅ = 0.0049(12); calculated from liquid P₂O₅ contents in runs 28C, 33C, and 42C (Table 3); phase proportions; and ol-liq, opx-liq, and cpx-liq partition coefficients for P₂O₅ of 0.1, 0.03, and 0.05 (Libourel *et al.*, 1994; Brunet & Chazot, 2001). Uncertainties (with the exception of those for K₂O and P₂O₅) are based on Monte Carlo propagations of errors on phase compositions and estimated weighing errors; uncertainty on K₂O and P₂O₅ is one sample standard deviation of the mean bulk K₂O and P₂O₅ values.

⁵Composition of Glass Buttes rhyolite taken from Dobson *et al.* (1989) and Ihinger *et al.* (1999).

nodules, ground, sieved to 16–28 mesh, cleaned in warm 2.4 N hydrochloric acid, and rinsed in deionized water. They were then crushed further, sieved to 200–325 mesh, and again washed in 2.4 N HCl and deionized water. Finally, the grains were ground and sieved to $\leq 13 \mu\text{m}$. The synthetic diopside was ground by hand until most of the grains were $< 15 \mu\text{m}$, but the powder still contained a few grains as large as $40 \mu\text{m}$ in size. The minerals were mixed in the weight proportions 0.432 KBH olivine, 0.202 H1801i olivine, 0.274 KBH orthopyroxene, 0.014 KBH clinopyroxene, 0.060 diopside, and 0.018 KBH spinel to generate the depleted peridotite starting material (DMM1). The mixture was ground by hand for 1 h under ethanol to ensure homogeneity.

The bulk composition of DMM1 in terms of major oxides is reported in Table 1. With the exceptions of K₂O and P₂O₅, these values were computed from the mineral compositions and their proportions in the mix (see preceding paragraph). K₂O and P₂O₅ contents for DMM1 were calculated using the K₂O and P₂O₅ contents of glasses in selected experiments, mineral–melt partition coefficients from the literature, and melt fractions and residual mineral proportions for these experiments derived from mass balance constraints using the other oxides (see footnotes to Tables 1 and 3).

The starting DMM1 composition was chosen to represent a moderately depleted mantle peridotite. When compared with the residues in the 10 kbar melting experiments of Baker & Stolper (1994) and Baker *et al.* (1995), DMM1 is roughly equivalent to the residue formed by 12–13% batch melting of MM3. Figure 1 compares the concentrations of MgO, Al₂O₃, CaO, and Na₂O in DMM1 with other peridotites studied experimentally at 9–10 kbar, with estimates of the primitive mantle, and with reconstructed abyssal peridotites. DMM1 has lower Al₂O₃, CaO, and Na₂O contents than all estimates of primitive mantle, and, unlike other peridotite compositions that have been studied experimentally, it falls on the well-defined MgO–oxide trends for abyssal peridotites (Fig. 1). Figure 1a and b shows that DMM1 is lower in Al₂O₃ than all other experimentally studied peridotite compositions and lower in CaO than the others, except those investigated by Sen (1982; 5 in Fig. 1b) and by Pickering-Witter & Johnston (2000; 9 in Fig. 1b; note that this composition is far removed from the MgO–CaO trend defined by abyssal peridotites and primitive mantle estimates). Figure 1c shows that DMM1 also has lower Na₂O than most peridotite compositions previously studied.

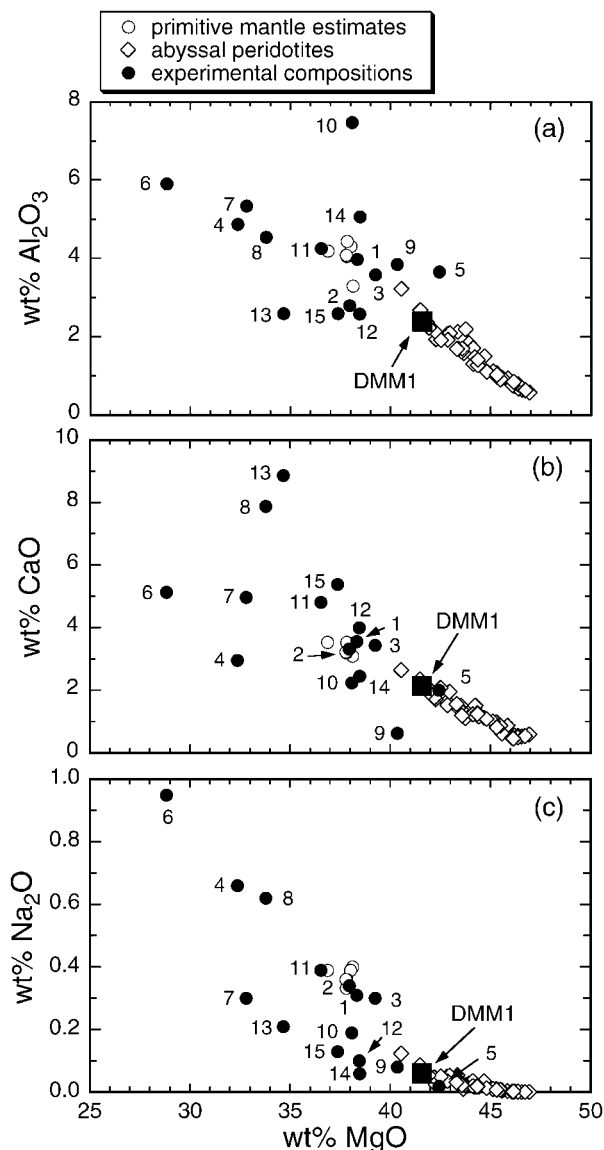


Fig. 1. MgO-oxide variation diagrams showing the bulk composition of the moderately depleted DMM1 peridotite used in this study (large filled square) and estimates of primitive upper-mantle compositions (○: Ringwood, 1979; Sun, 1982; Wänke *et al.*, 1984; Hart & Zindler, 1986; Allègre *et al.*, 1995; McDonough & Sun, 1995), reconstructed abyssal peridotite compositions (◇: Baker & Beckett, 1999), and other peridotitic starting materials studied experimentally at 9–10 kbar (●: 1, MM3, Baker & Stolper, 1994; 2, PHN1611, Kushiro, 1996; 3, KLB-1, 4, HK-66, Hirose & Kushiro, 1993; 5, 77PAII-1, Sen, 1982; 6, Hawaiian Pyrolite-40% olivine (HPy-40); 7, Tinaquillo Lherzolite-40% olivine, Jaques & Green, 1980; 8, FER-B, 9, FER-C, 10, FER-D, 11, FER-E, Pickering-Witter & Johnston, 2000; 12, INT-A, 13, INT-B, 14, INT-D, 15, INT-E, Schwab & Johnston, 2001). MgO vs (a) Al₂O₃, (b) CaO, (c) Na₂O.

Experimental methods

All experiments were run in a 1.27 cm piston cylinder apparatus using CaF₂ cells, straight-walled graphite furnaces, and inner pieces of crushable MgO dried at

1000°C for at least 8 h. Pressure was applied using the hot-piston-in technique with no friction correction. Experiments at 1300°C with identical assemblies bracketed the Ca-Tschermak breakdown reaction to lie at 11–14 kbar. This pressure range encompasses the reaction boundary (1300°C, 13 kbar) determined by Hays (1966). W₉₇Re₃/W₇₅Re₂₅ thermocouples were used to monitor and control temperature to within ~1°C of the set point. No pressure correction was applied to the nominal e.m.f.–temperature relation. Based on past experiments with double thermocouples, temperatures are estimated to be accurate to within ±15°C.

Run durations and experimental conditions are reported in Table 2. Except in experiments 1, 2, and 3, N₂ gas was bled into the slot in the thermocouple plate during each experiment to minimize oxidation of the thermocouple wires within and just below the steel base plug. At the end of each experiment, the thermocouple wires just below the base plug (i.e. within the run assembly) were inspected for signs of oxidation; no evidence of significant oxidation was observed on any of the wires, including those from experiments 1–3. After the power was turned off, samples cooled to below 1000°C within several seconds. As each run assembly was taken apart, the position of the capsule relative to the center of the furnace and that of the thermocouple junction relative to the top of the capsule were measured to ensure that the capsule was properly positioned within the furnace and that the thermocouple tip was 0.5–1 mm from the top of the capsule. Each capsule was sliced vertically with a diamond wafering blade, mounted in epoxy, and polished for electron microprobe analysis.

This study includes three types of melting experiments. The first type of experiment consisted of two stages (see Baker & Stolper, 1994). For the first stage, 3–6 mg of peridotite powder that had been dried in a vacuum oven at 110°C for ≥2 h was loaded into a graphite inner capsule. The inner capsule was then placed in a 0.15 inch o.d. Pt capsule. The composite capsule assembly was then dried (see Table 2); and finally the crimped end of the Pt capsule was welded. After drying and welding, the capsule was run at temperature and pressure for ~52–136 h. For the second stage, the silicate charge was removed from the first-stage capsule and loaded into a new graphite capsule along with 80–100 µm diameter vitreous carbon spheres that had been dried for at least 1 h in a 110°C vacuum oven. The mass of vitreous carbon (Table 2) was ~3–9% of the mass of the silicate sample. The loaded second-stage graphite capsule was then placed in a Pt capsule, after which the composite assembly was dried and welded shut. This second-stage capsule was then run for ~18–135 h at the same temperature and

Table 2: Experimental results

Run	Temp. (°C)	Drying*	1st stage (h)	2nd stage (h)	Silicate (mg)	Glassy carbon (mg)†	Phases present	Phase proportions (wt %) <dd>‡</dd>
9	1390	300/4,300/1	51.7	59.4	5.01	0.175	gl, ol, opx	16.6(6), 68.1(1.5), 15.4(1.6)
30	1370	400/1,400/1	69.5	87.5	4.85	0.196	gl, ol, opx	13.6(5), 68.1(1.7), 18.3(1.7)
1	1350	110/12+,110/3	72.1	18.5	4.17	0.261	gl, ol, opx	12.5(6), 67.5(1.5), 20.0(1.6)
2	1330	110/20,300/2	93.4	37.6	4.32	0.238	gl, ol, opx	10.0(5), 67.1(1.5), 22.9(1.6)
20C	1330	110/12+	141.3		3.07	0.435 (33.8, FB)	gl, ol, opx	11.7(4), 66.9(1.5), 21.4(1.5)
26C	1325	450/2	166.0		4.38	(9.8, GBR)	gl, ol, opx	12.3(5), 66.6(1.4), 21.1(1.5)
25T	1285/1325	110/12+	30.2/92.8		3.02	0.277	gl, ol, opx	10.8(5), 66.0(1.5), 23.2(1.7)
23T	1310/1325	300/1	25.5/87.8		3.83	0.198	gl, ol, opx, cpx	8.8(5), 66.5(7), 23.5(8), 1.2(4)
3	1310	110/3,110/12+	93.9	39.1	4.36	0.183	gl, ol, opx	10.3(5), 66.8(1.5), 22.9(1.7)
22	1300	300/1,110/3	116.4	114.7	4.61	0.403	gl, ol, opx, cpx, sp	6.6(8), 65.0(1.6), 24.0(1.7), 4.2(7), 0.3(2)
17T	1285/1300	300/1	68.4/117.2		3.56	0.252	gl, ol, opx, cpx, sp	3.2(8), 65.5(1.5), 25.3(1.7), 5.8(7), 0.3(1)
12	1290	300/1,300/2	92.9	70.5	2.69	0.078	gl, ol, opx, cpx, sp	6.4(7), 66.4(1.4), 23.5(1.6), 3.4(7), 0.3(1)
27C	1290	450/2	126.8		4.82	(21.6, FB)	gl, ol, opx, cpx, sp	5.4(8), 64.1(1.8), 26.3(2.0), 3.7(7), 0.5(2)
28C	1290	400/2	141.5		4.15	(26.9, FB)	gl, ol, opx, cpx, sp	2.6(7), 64.5(1.5), 26.8(1.6), 5.8(8), 0.4(2)
33C	1275	400/4	161.7		3.78	(22.0, FB)	gl, ol, opx, cpx, sp	1.6(3), 64.7(1.3), 26.5(1.4), 6.8(5), 0.5(2)
34C	1275	400/5	188.5		4.74	(40.6, GBR)	gl, ol, opx, cpx, sp	4.0(8), 64.7(1.4), 26.0(1.6), 5.0(7), 0.3(2)
42C	1270	400/4	184.3		5.88	(31.8, FB)	gl, ol, opx, cpx, sp	3.3(6), 62.6(1.6), 27.9(1.7), 5.4(5), 0.8(2)
36	1250	400/4,400/4	142.0	245.5	9.26		ol, opx, cpx, sp	62.8(1.7), 28.4(1.9), 8.1(5), 0.6(2)§

Phases present: gl, glass; ol, olivine; opx, orthopyroxene; cpx, clinopyroxene; sp, spinel.

*Indicates drying procedure for loaded capsule before welding. Temperature and duration in hours (rounded to nearest hour; 12+ indicates that the capsule was dried overnight) separated by slash. Drying conditions for both stages given for two-stage runs.

†Numbers in parentheses indicate masses, in micrograms, of aggregate chips included with silicate samples in compositional-convergence runs. FB and GBR indicate glass used in aggregate chip; FB, synthetic ferrobaltic glass; GBR, Glass Buttes rhyolite (compositions listed in Table 1).

‡Calculated by mass balance. Numbers in parentheses indicate uncertainties; e.g. 16.6(6) represents $16.6 \pm 0.6\%$ liquid. The silica contents of 17 of the 18 olivine compositions used to calculate the modes have been adjusted using the stoichiometric constraint for ol that Si (cation %) equals 33.333. For each of these analyses, the SiO_2 (wt %) value was iteratively raised or lowered and cation % calculated until the Si value was within 0.005 units of 33.333. All oxides were then normalized to 100 wt %; it should be noted that this procedure has no effect on the Mg/(Mg + Fe) ratio of the olivines. Although the correction is relatively small (e.g. mean absolute value of the change in silica contents is 0.26 wt %), the correlation coefficients for melt fraction (F) vs ol and F vs opx increased dramatically (e.g. for F vs ol, the Pearson correlation coefficient increased from 0.05 to 0.58). Unadjusted olivine compositions are reported in Table 3.

§Calculated using analyses for opx and cpx that were normalized to 100 wt % (see Table 3).

pressure as its corresponding first-stage run. At the end of each second-stage experiment, the charge contained quenched glass associated with the vitreous carbon. The glass formed rinds generally 3–15 μm thick around individual vitreous carbon spheres. Varying amounts of glass and crushed carbon spheres filled the spaces between the intact spheres (Fig. 2a). The idea behind this type of experiment was to avoid the possibility of formation and segregation of disequilibrium liquids at the start of the experiment that would not subsequently equilibrate with the main mass of the sample. In two-stage experiments, liquids maintain intimate contact with the peridotite and approach equilibrium during the first stage and are segregated only in the second stage.

The second type of experiment was run as a single stage, but the temperature was changed during the experiment to evaluate whether liquid that had segregated into the interstices between the vitreous carbon spheres could respond chemically to changes in temperature; these experiments are indicated by a T next to the run number in Table 2. Graphite capsules were loaded with vitreous carbon and peridotite powder, placed in Pt outer capsules, and then dried and welded shut as for the previously described charges. Each sample was run at 10 kbar and an initial temperature as listed in Table 2 for ~26–68 h. Following this initial period, the temperature was raised either 15 or 40°C, and the charge was held at this higher temperature for an additional ~88–117 h. The potential concern

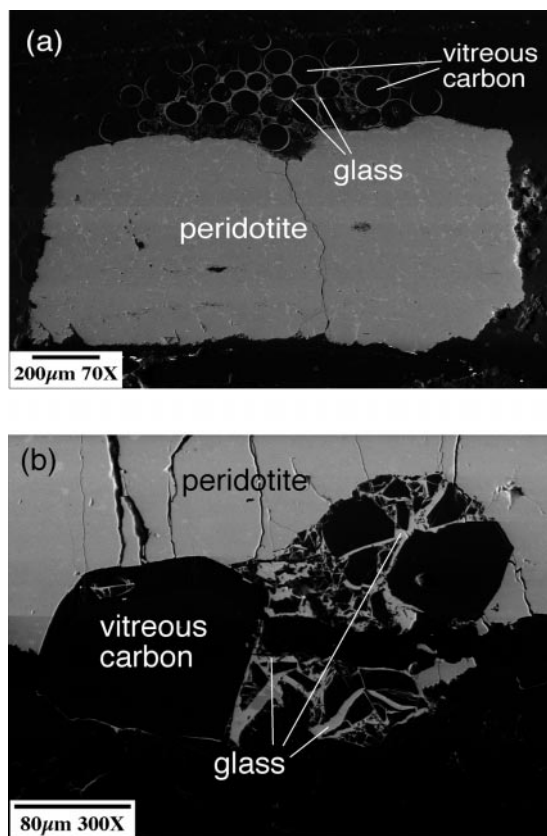


Fig. 2. Backscattered electron photomicrographs of (a) a typical charge with vitreous carbon spheres and (b) a portion of the charge from run 28C, showing the chip of vitreous carbon aggregate that had been pre-impregnated with ferrobasalt before the experiment.

addressed by these experiments is whether liquid segregated into the vitreous carbon at the start of the experiment is in sufficient chemical contact with the main mass of the experimental charge that its composition can change by diffusive interaction with the peridotite and its interstitial liquid.

We refer to the third type of experiment as 'compositional-convergence' runs; these experiments are marked with a C next to the run number in Table 2. For these seven experiments, glass-bearing vitreous carbon aggregates were prepared as follows. An oxide mix of a synthetic ferrobasalt or a powdered rhyolitic glass from Glass Buttes, Oregon (both compositions are reported in Table 1), were mixed with conchoidally fractured vitreous carbon shards (80–147 μm in size). Approximately 85% (by weight) of the material in each capsule was vitreous carbon. Each of these two mixtures was loaded into a separate Pt capsule and then held at 10 kbar and 1350°C for a few hours. At the end of these two preparatory runs, the silicate liquids had impregnated most of the pore spaces between the vitreous carbon fragments. Fragments (10–41 μg ; see

Table 2) of the glass-impregnated vitreous carbon aggregates were loaded into graphite–Pt capsules with DMM1 powder ($\sim 3\text{--}6\text{ mg}$; see Table 2) as described above for the other two types of experiments. The samples were run for $\sim 127\text{--}188\text{ h}$. In one experiment (20C), a layer of vitreous carbon spheres was also loaded into the capsule at the opposite end of the charge from the ferrobasalt-impregnated vitreous carbon aggregate. The purpose of these experiments was to examine the degree to which the ferrobasaltic and rhyolitic glasses in the interstices of the vitreous carbon aggregate were able to converge in composition toward each other and toward the compositions of glasses within vitreous carbon aggregates that were not pre-filled with glass (i.e. glass within the layer of vitreous carbon in 20C or that in charges from the previously described experiments). Because the ferrobasaltic and rhyolitic glasses are extremely distant in composition from the equilibrium partial melts of the DMM1 peridotite, the extent to which they can shift compositionally during an experiment can be used to demonstrate that liquids segregated into vitreous carbon aggregates can maintain chemical contact with the main mass of the peridotite during an experiment. This means that even if a disequilibrium liquid migrates into the vitreous carbon aggregate at the start of an experiment, it can evolve substantially via exchange with the bulk charge over the course of the experiment. Moreover, if the initial ferrobasaltic and rhyolitic compositions converge to a single composition similar to glasses from our two-stage and temperature-change experiments, we can infer with confidence that an equilibrium liquid composition was approached closely.

Oxygen fugacity was not controlled in our experiments, but the presence of graphite inner capsules constrains f_{O_2} to below the graphite–CO vapor buffer (GCO). Following the approach discussed by Bertka & Holloway (1988) and Gudmundsson *et al.* (1988), we placed 13 μg of platinum wire in the middle of the peridotite powder in experiment 25 (1325°C). During the experiment the Pt wire absorbed Fe. Based on the compositions of the resulting Fe–Pt alloy and coexisting orthopyroxene and olivine, and using the equations and solution models of Jamieson *et al.* (1992), the $\log_{10} f_{\text{O}_2}$ in run 25 was -9.2 , or ~ 2.4 log units below the quartz–fayalite–magnetite buffer (QFM) at 10 kbar (Huebner, 1971). The slightly different activity–composition models of Gudmundsson & Holloway (1993) yielded a $\log_{10} f_{\text{O}_2}$ of -8.5 , or ~ 1.7 log units below QFM. The inferred f_{O_2} values of our experiments are thus consistent with estimates for the MORB source region (Christie *et al.*, 1986; Green *et al.*, 1987; O'Neill & Wall, 1987; Mattioli & Wood, 1988; Mattioli *et al.*, 1989).

Analytical techniques

Experimental charges were analyzed at Caltech with a five spectrometer JEOL 733 electron microprobe using an accelerating voltage of 15 keV. Crystalline phases in all experiments (including the Pt alloy in run 25) were analyzed with a beam current of 30 nA and a rastered beam at magnifications greater than 40 000 \times (the resulting spot size is less than 2 μm \times 2 μm). Glasses were analyzed with a 2.5, 5, or 10 nA beam current and a rastered area as large as possible for the glass pools being analyzed (generally $\sim 5 \mu\text{m}$ \times 5 μm). Repeated analyses on the same region of glass within several experiments indicated little or no Na loss. All data were processed using CITZAF (Armstrong, 1988). Two basaltic glasses, VG-2 and BGIO (Jarosewich *et al.*, 1979), were analyzed as secondary standards during each microprobe session to estimate accuracy and precision of the instrument on a long-term basis; when crystalline phases were analyzed, Johnstown hypersthene and Natural Bridge diopside (Jarosewich *et al.*, 1979) were also analyzed to provide additional estimates of accuracy and precision.

Raw oxide sums for the experimental glasses were typically 95–97%, but were occasionally lower, and in one case down to 89%. We consistently observed higher totals for glass pools that were more than $\sim 5 \mu\text{m}$ in the shortest dimension and lower totals for smaller glass pools. The low totals probably reflect the inclusion of vitreous carbon in the electron beam analysis volume. This inference is supported by the observation that when all of the glass analyses for a given sample are normalized to 100%, there are no systematic differences in the normalized oxide concentrations as functions of the raw oxide sums. Within the vitreous carbon aggregate of a given experiment, normalized glass compositions display no systematic variation as a function of distance from the DMM1 peridotite. Mean compositions for normalized glasses, crystalline phases, and secondary standards are reported in Table 3.

Water contents of the glasses in two charges (3 and 22) were measured by secondary ion mass spectrometry with the modified Cameca IMS-3f ion microprobe at Lawrence Livermore National Laboratories using the techniques described by Kent *et al.* (1999). Measured $\text{H}^+ / ^{30}\text{Si}^+$ ratios in our experimental glasses were converted to water contents with a calibration curve constructed by analyzing a set of Marianas back-arc basin basaltic glasses (Stolper & Newman, 1994) and synthetic MORB glasses (Dixon *et al.*, 1995) whose water and silica contents were determined by independent techniques. Errors on the water contents of the experimental glasses are conservatively estimated at $\pm 15\%$ relative. Charges 3 and 22 contain 1.2 ± 0.2 and 0.3 ± 0.1 wt % water, respectively. These have not been

corrected for the possible effects of vitreous carbon in the analysis volume. As vitreous carbon can dissolve hydrogen in the presence of water-bearing melt, but contains no Si (L. Wasylenki, unpublished data, 1995), such a correction would probably lead to lower estimates of the water contents of our experimental glasses.

RESULTS

Evaluation of the approach to equilibrium

Although the melt-extraction technique used in this study provides a simple way to avoid the quench modification problems encountered in conventional peridotite melting experiments close to the solidus, the technique must be applied with care. In particular, the issue of whether the glasses within the vitreous carbon aggregates (this study; Pickering-Witter & Johnston, 2000; Schwab & Johnston, 2001) or diamond aggregates (e.g. Johnson & Kushiro, 1992; Hirose & Kushiro, 1993; Baker & Stolper, 1994; Baker *et al.*, 1995; Kushiro, 1996) actually represent equilibrium melt compositions has sparked much debate (Baker *et al.*, 1996; Falloon *et al.*, 1996, 1997, 1999; Wasylenki *et al.*, 1996). For example, as explained above, one possible problem with the one-stage experiments of Baker & Stolper (1994) is that at the onset of an experiment, low pore pressure within the diamond layer could affect the composition of liquid initially filling these pores, i.e. the initial liquid may not be in equilibrium with the bulk peridotite at the nominal pressure of the experiment. Similarly, the kinetics of melting could lead to generation of a disequilibrium liquid at the start of an experiment. In either of these cases, liquid migrating rapidly into the pores in the diamond or vitreous carbon layer might not be in equilibrium with the bulk of the material in the capsule, and, if this segregated liquid were subsequently cut off from exchange with the adjacent peridotite, results would be erroneous. Liquids segregated into diamond aggregates in short-duration, one-stage experiments do indeed differ from those produced in long-duration runs at the same temperature and pressure (Johnson & Kushiro, 1992; Baker & Stolper, 1994), so this general class of potential problems cannot be disregarded. Our two-stage experiments, however, were designed to minimize these problems in that the liquid moving into a vitreous carbon layer at the beginning of a second-stage run is remelted glass from the first-stage run and thus should represent a near-equilibrium melt.

Temperature-change experiments

Although our two-stage experiments were explicitly designed to minimize problems of melt re-equilibration

Table 3: Experimental results

Run	Phase	SiO ₂	TiO ₂	Al ₂ O ₃	Cr ₂ O ₃	FeO*	MnO	MgO	CaO	Na ₂ O	K ₂ O	Sum
9	gl(6)	50.96(26)	0.17(11)	12.19(11)	0.38(6)	8.36(18)	0.19(7)	16.58(22)	10.65(24)	0.44(3)	0.08(1)	100
	ol(5)	41.36(18)	0.01(1)	0.05(1)	0.25(2)	8.94(9)	0.13(2)	49.67(26)	0.24(2)	—	—	100.65
	opx(12)	56.70(24)	0.02(2)	1.83(21)	0.81(6)	5.26(13)	0.11(2)	33.75(21)	1.30(14)	0.02(1)	—	99.80
30	gl(5)	50.38(37)	0.25(8)	12.87(15)	0.42(7)	7.93(31)	0.22(6)	15.43(25)	12.18(19)	0.30(3)	0.02(1)	100
	ol(8)	40.96(15)	—	0.05(1)	0.27(3)	8.96(12)	0.13(2)	49.15(38)	0.27(1)	—	—	99.79
	opx(11)	55.73(20)	0.03(2)	3.00(26)	0.84(8)	5.62(8)	0.12(2)	32.22(26)	1.82(6)	0.02(1)	—	99.40
1	gl(6)	50.21(21)	0.21(4)	14.15(13)	0.36(5)	7.72(17)	0.15(4)	14.35(17)	12.23(19)	0.55(3)	0.07(1)	100
	ol(6)	40.92(15)	—	0.04(1)	0.24(2)	8.96(9)	0.14(3)	49.23(26)	0.24(2)	—	—	99.77
	opx(8)	55.39(42)	0.02(1)	2.94(28)	0.94(5)	5.73(20)	0.10(2)	32.55(34)	1.93(17)	0.02(1)	—	99.62
2	gl(9)	49.45(21)	0.28(8)	15.43(14)	0.27(5)	7.34(16)	0.16(7)	12.77(20)	13.61(22)	0.60(4)	0.08(1)	99.99
	ol(3)	41.30(15)	—	0.04(1)	0.21(2)	9.24(9)	0.12(2)	49.26(26)	0.31(1)	—	—	100.48
	opx(4)	54.86(38)	0.04(2)	3.58(25)	0.98(6)	5.68(18)	0.10(2)	31.93(34)	2.45(7)	0.02(1)	—	99.64
20C	gl in vc(4)	49.50(24)	0.33(8)	14.92(13)	0.31(5)	7.34(16)	0.10(3)	13.49(16)	13.23(21)	0.67(5)	0.10(1)	100
	gl in ic(4)	49.38(21)	0.32(9)	15.15(14)	0.30(5)	7.37(16)	0.11(4)	13.32(16)	13.25(21)	0.70(1)	0.09(1)	100
	ol(9)	40.88(18)	—	0.05(1)	0.21(2)	9.21(10)	0.13(2)	48.98(26)	0.30(1)	—	—	99.76
26C	opx(6)	56.12(20)	0.03(1)	2.53(16)	0.78(5)	5.69(9)	0.13(2)	32.97(18)	2.18(6)	0.02(1)	—	100.45
	gl(6)	50.19(28)	0.27(4)	13.78(14)	0.27(4)	7.81(21)	0.15(7)	14.10(33)	12.81(20)	0.56(3)	0.07(2)	100
	ol(8)	40.62(15)	—	0.06(2)	0.16(1)	9.32(11)	0.14(3)	49.36(30)	0.27(1)	—	—	99.93
25T	opx(7)	55.95(22)	0.02(2)	2.56(26)	0.91(7)	5.79(8)	0.10(2)	32.79(29)	1.81(9)	0.02(1)	—	99.95
	gl(7)	49.21(24)	0.30(4)	14.16(14)	0.23(3)	7.61(17)	0.11(4)	14.18(17)	13.55(21)	0.56(3)	0.07(1)	100
	ol(4)	41.11(29)	—	0.05(2)	0.19(2)	9.13(19)	0.13(2)	49.24(29)	0.30(1)	—	—	100.15
23T	opx(4)	55.94(20)	0.02(2)	2.78(30)	0.74(9)	5.66(14)	0.13(2)	32.59(18)	2.10(9)	0.02(1)	—	99.98
	gl(7)	48.99(24)	0.28(9)	15.37(17)	0.22(6)	7.91(17)	0.09(5)	12.60(29)	13.66(22)	0.81(10)	0.07(1)	100
	ol(8)	40.84(15)	—	0.05(1)	0.17(3)	9.44(10)	0.14(3)	49.60(26)	0.29(3)	—	—	100.53
3	opx(6)	54.86(20)	0.05(2)	3.65(22)	0.98(5)	5.82(7)	0.12(2)	32.07(27)	2.32(7)	0.03(1)	—	99.90
	cpx(6)	52.10(28)	0.03(2)	5.10(19)	1.34(8)	3.80(11)	0.11(2)	20.02(26)	17.04(30)	0.12(2)	—	99.66
	gl(11)	49.64(21)	0.28(4)	15.12(14)	0.29(4)	7.41(16)	0.13(3)	13.32(16)	13.12(21)	0.60(3)	0.08(1)	100
22	ol(9)	41.13(15)	—	0.04(1)	0.19(4)	9.25(11)	0.13(2)	49.07(26)	0.28(1)	—	—	100.09
	opx(2)	55.30(52)	0.05(1)	3.24(10)	0.79(4)	5.63(15)	0.10(2)	31.69(17)	2.54(13)	0.03(1)	—	99.37
	gl(7)	48.08(51)	0.39(6)	17.73(20)	0.17(3)	7.07(16)	0.18(5)	12.02(30)	13.32(21)	0.96(5)	0.08(1)	100
17T	ol(5)	39.58(21)	—	0.07(4)	0.18(5)	9.45(9)	0.14(3)	49.67(26)	0.27(2)	—	—	99.36
	opx(4)	55.22(45)	0.01(1)	2.44(23)	0.83(10)	5.85(7)	0.10(2)	33.35(18)	1.68(13)	0.02(1)	—	99.50
	cpx(4)	50.89(30)	0.12(3)	6.27(36)	1.00(5)	3.91(12)	0.10(2)	19.95(38)	16.82(22)	0.14(2)	—	99.20
12	sp(2)	0.29(2)	0.11(2)	34.19(32)	35.95(54)	10.35(10)	0.14(3)	18.66(10)	0.02(1)	0.01(1)	—	99.72
	gl(11)	48.81(35)	0.39(18)	16.89(15)	0.19(7)	7.28(24)	0.14(9)	12.14(14)	12.85(20)	1.14(5)	0.17(2)	100
	ol(10)	40.81(15)	—	0.05(1)	0.13(1)	9.60(14)	0.14(3)	48.71(26)	0.27(1)	—	—	99.71
27C	opx(5)	54.24(54)	0.08(2)	4.83(46)	0.79(7)	5.84(7)	0.13(2)	31.57(39)	2.18(11)	0.05(2)	—	99.71
	cpx(4)	52.07(39)	0.11(3)	5.47(16)	1.02(7)	3.83(13)	0.11(2)	20.03(38)	17.39(38)	0.21(3)	—	100.24
	sp(3)	0.60(52)	0.09(2)	47.62(43)	21.89(23)	8.92(9)	0.11(2)	20.35(37)	0.05(1)	—	—	99.63
12	gl(11)	48.88(20)	0.41(10)	17.61(16)	0.19(5)	6.84(15)	0.16(5)	11.72(16)	13.21(21)	0.84(4)	0.14(2)	100
	ol(8)	40.83(15)	—	0.03(1)	0.11(1)	9.42(13)	0.14(3)	49.15(26)	0.25(1)	—	—	99.93
	opx(4)	55.30(20)	0.04(2)	3.49(26)	0.92(9)	5.78(7)	0.12(2)	32.27(39)	2.25(21)	0.02(1)	—	100.19
27C	cpx(4)	52.46(34)	0.08(2)	5.23(51)	1.15(5)	3.80(8)	0.12(2)	20.00(36)	17.80(41)	0.15(2)	—	100.79
	sp(2)	0.26(7)	0.06(3)	44.60(95)	25.1(1.1)	9.32(42)	0.12(4)	20.06(11)	0.02(1)	—	—	99.55
	gl(13)	48.22(20)	0.48(7)	15.95(16)	0.12(4)	7.30(21)	0.09(6)	12.75(26)	13.89(22)	1.12(6)	0.09(2)	100
27C	ol(5)	40.82(30)	—	0.05(1)	0.08(1)	9.56(9)	0.13(2)	49.07(44)	0.24(1)	—	—	99.95
	opx(8)	55.02(48)	0.05(1)	3.70(14)	0.88(15)	5.98(11)	0.12(2)	31.66(17)	2.21(10)	0.04(2)	—	99.66

Run	Phase	SiO ₂	TiO ₂	Al ₂ O ₃	Cr ₂ O ₃	FeO*	MnO	MgO	CaO	Na ₂ O	K ₂ O	Sum
28C	cpx(10)	52.17(46)	0.09(2)	5.15(54)	1.20(12)	3.82(9)	0.10(2)	18.72(24)	18.04(33)	0.18(3)	—	99.47
	sp(2)	0.39(32)	0.09(2)	39.8(1.5)	30.1(2.1)	10.51(17)	0.13(2)	19.73(60)	0.04(1)	—	—	100.79
	gl(6)	48.07(20)	0.58(25)	15.92(25)	0.15(6)	7.54(18)	0.15(6)	12.35(19)	13.72(22)	1.38(10)	0.14(2)	100
	ol(4)	41.01(15)	—	0.07(1)	0.09(3)	9.65(13)	0.13(2)	48.44(29)	0.30(3)	—	—	99.69
	opx(6)	53.76(27)	0.07(2)	5.01(36)	0.80(5)	6.05(11)	0.12(2)	31.35(17)	2.26(10)	0.04(2)	—	99.46
	cpx(4)	51.72(37)	0.11(5)	5.61(42)	1.01(5)	3.88(15)	0.11(2)	19.07(65)	17.60(65)	0.28(3)	—	99.39
33C	sp(4)	0.84(17)	0.10(2)	48.8(1.0)	19.82(87)	9.29(17)	0.12(2)	20.90(15)	0.07(2)	—	—	99.94
	gl(10)	47.96(20)	0.63(8)	17.77(16)	0.09(3)	7.29(16)	0.13(4)	10.35(12)	13.19(21)	2.08(10)	0.51(1)	100
	ol(6)	40.99(15)	—	0.05(2)	0.08(2)	9.61(15)	0.12(3)	48.42(26)	0.24(1)	—	—	99.51
	opx(6)	54.28(20)	0.08(2)	5.04(22)	0.73(5)	5.99(7)	0.13(2)	31.19(17)	2.28(11)	0.04(1)	—	99.76
	cpx(4)	51.21(24)	0.16(3)	5.90(38)	0.97(5)	3.90(12)	0.10(2)	19.08(25)	17.84(14)	0.27(2)	—	99.43
	sp(2)	0.75(61)	0.12(3)	49.34(56)	19.2(1.1)	9.66(35)	0.14(5)	20.4(1.0)	0.07(4)	—	—	99.68
34C	gl(7)	48.83(20)	0.50(7)	16.87(15)	0.11(3)	7.19(16)	0.18(5)	11.51(22)	13.04(21)	1.43(7)	0.33(2)	100
	ol(4)	40.83(15)	—	0.04(1)	0.10(2)	9.72(20)	0.14(3)	48.08(26)	0.25(2)	—	—	99.16
	opx(8)	54.27(20)	0.04(1)	4.58(29)	0.88(12)	5.97(7)	0.12(2)	31.02(25)	2.18(9)	0.04(2)	—	99.10
	cpx(3)	51.75(54)	0.11(6)	4.74(24)	1.16(18)	3.89(9)	0.12(2)	19.30(30)	17.60(38)	0.31(14)	—	98.98
	sp(3)	0.82(42)	0.08(2)	48.2(1.5)	20.8(1.7)	9.58(9)	0.12(2)	19.92(18)	0.06(3)	—	—	99.58
	gl(7)	47.93(20)	0.59(7)	17.54(16)	0.11(3)	7.28(17)	0.13(4)	11.42(17)	13.25(21)	1.60(8)	0.14(2)	100
42C	ol(9)	40.59(15)	—	0.05(1)	0.08(2)	9.74(15)	0.13(2)	49.44(26)	0.23(1)	—	—	100.26
	opx(4)	54.17(40)	0.06(2)	3.93(12)	0.93(21)	5.91(16)	0.13(2)	32.45(50)	2.19(6)	0.04(2)	—	99.81
	cpx(6)	51.83(19)	0.09(2)	4.87(37)	1.21(5)	3.76(9)	0.11(2)	19.71(40)	18.07(25)	0.17(3)	—	99.82
	sp(3)	0.49(23)	0.11(2)	42.4(1.7)	28.5(1.8)	10.19(13)	0.14(3)	19.73(24)	0.05(3)	—	—	101.61
	ol(9)	40.84(18)	—	0.07(5)	0.06(2)	9.70(11)	0.13(2)	49.07(30)	0.14(4)	—	—	100
	opx(7) ¹	54.03(65)	0.07(2)	4.80(25)	0.71(8)	6.09(15)	0.13(2)	32.17(52)	1.95(11)	0.05(2)	—	100
36	cpx(16) ¹	51.71(40)	0.19(6)	5.74(32)	0.98(8)	3.67(15)	0.10(2)	18.67(60)	18.52(33)	0.42(15)	—	100
	sp(3)	1.21(1.03)	0.10(1)	47.74(74)	20.37(93)	10.24(21)	0.13(2)	19.30(24)	0.11(14)	0.01(1)	—	99.21
VG2(176) ²		50.40(43)	1.80(12)	13.93(20)	0.02(3)	11.55(21)	0.20(4)	6.89(11)	10.88(15)	2.79(8)	0.21(2)	98.66
BGIO(167)		51.30(49)	1.28(10)	15.19(24)	0.05(3)	8.98(20)	0.16(4)	8.04(14)	11.14(20)	2.78(14)	0.09(2)	99.01
JHYP(103)		54.46(46)	0.08(2)	0.85(4)	0.78(4)	14.72(25)	0.48(3)	27.33(22)	1.16(5)	0.01(1)	0.01(1)	99.88
DIOP(116)		55.60(52)	0.02(2)	0.20(10)	0.02(2)	0.29(3)	0.03(2)	18.06(21)	25.69(37)	0.17(6)	0.01(1)	100.09

C, compositional-convergence experiment; T, temperature-change experiment (see text for further discussion); gl, glass; ol, olivine; opx, orthopyroxene; cpx, clinopyroxene; sp, spinel; vc, layer of vitreous carbon spheres; ic, impregnated vitreous carbon chip; FeO*, all Fe as FeO. Numbers in parentheses after each phase are the number of analyses averaged for that phase; numbers in parentheses after each oxide value are 1 σ of the sample distribution in terms of the least units cited, e.g. 50.94(26) represents 54.94 \pm 0.26. Glass compositions normalized to 100% on a volatile-free basis. Measured H₂O contents for glasses from runs 3 and 22 are 1.2(2) and 0.3(1) wt %, respectively. Measured P₂O₅ contents in glasses from runs 28C, 33C, and 42C are 0.11(5), 0.16(1), and 0.12(2) wt %, respectively. Dashes indicate that the element was not analyzed or was below the detection limit.

¹Reported analyses have been normalized to 100 wt %. Repeated attempts to analyze the silicate phases in this charge consistently produced low analytical totals. The opx and cpx compositions reported here have nominal sums of 98.6 and 98.9 wt %, respectively. Following the calculations outlined by Cameron & Papike (1981), both compositions have acceptable pyroxene stoichiometries.

²Secondary standards. VG2, basaltic glass, Juan de Fuca Ridge; BGIO, basaltic glass, Indian Ocean; DIOP, diopside, Natural Bridge; JHYP, hypersthene, Johnstown meteorite (Jarosewich *et al.*, 1979). Mean oxide values for VG2 and BGIO analyzed during glass-analysis and mineral-analysis microprobe sessions, respectively, overlap at the 1 σ level. Thus, all VG2 analyses have been averaged together as have all BGIO analyses.

in the vitreous carbon layers, we nevertheless made further efforts to demonstrate directly that liquids in the vitreous carbon layers in our experiments can change composition over the course of an experiment. The temperature-change experiments described above provide evidence of continued interaction between

segregated melt and the peridotite over the course of an experiment.

We conducted three temperature-change experiments to demonstrate that segregated liquids can change composition in response to changes in experimental conditions. In each such experiment, after

initial run durations of 26–68 h at 1285 or 1310°C, temperatures were raised either 15 or 40°C and the runs continued for an additional 88–117 h. We assume that during the initial stages of these experiments, liquids in the vitreous carbon layers approached the glass compositional trends defined by the two-stage experiments at the same initial temperatures. In two of the three temperature-change experiments (17T, 1285–1300°C; 25T, 1285–1325°C), the final liquid compositions are similar to those in two-stage experiments run at the same final temperatures and different from liquid compositions expected at 1285°C (see Fig. 4). (The third experiment, 23T, appears to have had a significant temperature gradient, as evidenced by modal variations from top to bottom of the charge, and to have had a final temperature of ~1310°C rather than 1325°C; see the section ‘Phase relations and liquid compositions’ below.) Based on mass balance calculations using the quenched glass and mineral compositions and the bulk DMM1 composition, the melt fractions of 17T and 25T during their respective high-temperature steps were ~0.03 and 0.11 (Table 2). Thus, over the course of 93–117 h *at these melt fractions*, the segregated liquids in the vitreous carbon layers were able to change in response to the increase in temperature via diffusive exchange with liquid retained in the peridotite. We also attempted temperature-change experiments in which the temperature was lowered in the second phase of the experiment, but, as one would expect, this resulted in extensive crystallization within the vitreous carbon aggregates.

Compositional-convergence experiments

Successful ‘compositional-convergence’ experiments demonstrate not only that liquids in vitreous carbon aggregates can change significantly, but also by convergence that an equilibrium result has been approached from more than one direction in multi-component composition space. As described above, these experiments involved placing ~10–41 µg of a vitreous carbon aggregate that was pre-impregnated with either a synthetic ferrobalt or a rhyolite in a capsule with DMM1 powder (Fig. 2b). Based on the results of our two-stage experiments, both the ferrobalt and the rhyolite glass compositions were initially far from equilibrium with DMM1 at 10 kbar and any temperature. With the exceptions of K₂O and, to a lesser extent, Na₂O for the two rhyolite-bearing experiments, the few micrograms of glass added to the system have little effect on the bulk composition. The potassium budget in the two rhyolite-bearing runs (26C and 34C) is dominated by the rhyolite glass; for example, we estimate that the bulk K₂O content in 34C increased from ~0.006 wt %

(the estimated bulk composition of DMM1) to ~0.02 wt % as a result of the addition of the rhyolite-bearing vitreous carbon aggregate. The change in the sodium content in run 34C is less extreme; the Na₂O concentration increased from ~0.06 to ~0.07 wt %.

Figure 3 illustrates the large shifts in composition that the ferrobaltic and rhyolitic glasses underwent as a result of diffusive equilibration with 2–12 wt % melt in the peridotite and shows that the quenched liquids in all of these experiments define a single compositional trend approached from opposite directions in most compositional dimensions. As shown in Fig. 4, this compositional trend is consistent with the trend defined by glass compositions from the two-stage and temperature-change experiments. It is important to emphasize that the compositions of the liquids in the vitreous carbon chips in these experiments have converged to their final compositions from opposite directions in terms of several oxides and that the compositional changes achieved in these experiments are in some cases very large (e.g. SiO₂, CaO, MgO, and FeO* for the initially rhyolitic liquid). It is also striking that three of the convergence experiments are within <5°C of our estimated solidus for the DMM1 composition and have only ~2–5% melt (Table 2). These results should thus dispel controversy about the validity of melt-segregation experiments into diamond or vitreous carbon aggregates, as they demonstrate large compositional shifts, convergence from melts initially in the aggregates that are extremely far in composition from the final compositions, and that the results of two-stage, temperature-change, and ‘compositional-convergence’ experiments form coherent compositional trends as a function of melt fraction near the solidus.

Homogeneity of crystalline phases

We have also examined the compositions of the residual peridotite minerals in all of our experiments (Table 3), as true achievement of equilibrium would require homogeneous crystals and mineral compositions that are independent of distance from the glass-bearing aggregates.

In all experiments olivine grains (15–40 µm in size) were homogeneous within analytical error in each charge, both from core to rim of individual analyzed grains and from top to bottom of the residual peridotite.

Orthopyroxene grains with cross-sectional diameters larger than ~10 µm often displayed small, incompletely reacted cores, visible with high-gain, backscattered electron imaging. We estimate that these cores occupy <35% of the volume of *opx* in a given charge. The cores have compositions between the initial KBH *opx*

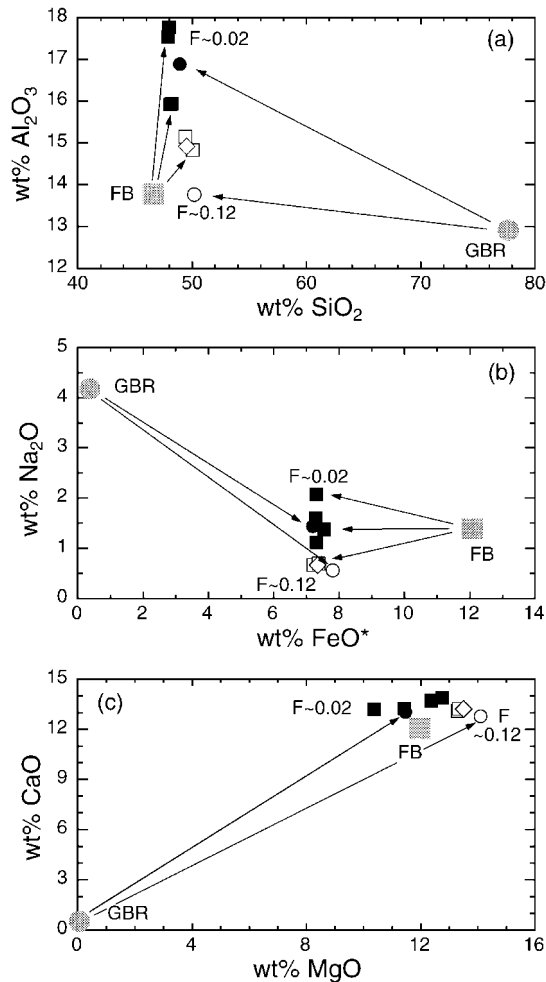


Fig. 3. Changes in melt compositions in ‘compositional-convergence’ experiments (see text): (a) SiO₂ vs Al₂O₃; (b) FeO* (all Fe as FeO) vs Na₂O; (c) MgO vs CaO. The large gray square in each panel represents the initial composition of ferrobaltic glass in aggregates of vitreous carbon particles that were loaded in capsules with DMM1 powder and run at 10 kbar for 127–184 h. Smaller open and filled squares represent compositions of glasses in the vitreous carbon chips at the end of the experiments. Glass composition from the vitreous carbon layer in run 20C is also plotted (◇). The large gray circle in each panel represents the initial composition of Glass Buttes rhyolite in another set of vitreous carbon aggregates run with DMM1 powder at 10 kbar for 166–188 h; smaller open and filled circles represent the compositions of the glasses at the end of these experiments. Glass compositions denoted by small filled squares or circles coexist with spinel lherzolite; small open squares or circles denote harzburgite residues. Arrows show typical compositional changes in these ‘compositional-convergence’ experiments; no arrows are drawn from the initial ferrobaltic composition to the re-equilibrated melts in (c) because of the close proximity of the two sets of symbols. Melt fractions (*F*) are given for the experiments that define each end of the compositional trends.

composition and analyzed rim compositions, indicating some compositional change toward equilibrium. We did not observe any significant differences in *opx* core and rim compositions as a function of distance

from the vitreous carbon aggregates in any of our experiments.

Clinopyroxene grains are typically <15 μm in size. Unreacted *cpx* cores were not clearly visible in back-scattered electron images, but microprobe analyses indicate that *cpx* grains in the run products are chemically heterogeneous. In particular, CaO and Al₂O₃ contents vary within and among the *cpx* grains in each charge. In our study, more than 20 *cpx* analyses were collected from each charge, and those that clustered toward the low-Al and low-Ca end of the trend in Al₂O₃–CaO–MgO space defined by all analyses within a charge were averaged for Table 3. None of the *cpx* analyses from any of the run products were close in composition to the starting KBH *cpx* composition or pure diopside, suggesting that all of the *cpx* in our experiments at least partially re-equilibrated. We did not observe any systematic variations in *cpx* compositions as a function of distance from the vitreous carbon aggregates, but in some experiments modal *cpx* abundance increases with increasing distance from the top of the capsule (i.e. the end closest to the thermocouple junction). The experiments in which this modal variation occurs probably experienced larger thermal gradients than those experiments that show a more uniform *cpx* distribution (Leshner & Walker, 1988).

Spinel is a minor phase in our experiments and, as run temperatures fall, shows more compositional heterogeneity within runs than olivine or pyroxenes. Spinel grains in the run products are small (<10 μm in size), and generally only 3–6 grains are visible on the polished surface of each charge. Thus we were not able to assess the degree of compositional variation within individual *sp* grains or as a function of the position of *sp* grains in the charge relative to the melt-bearing vitreous carbon aggregates. We did observe that in a given charge, grains of *sp* in direct contact with melt tended to be more compositionally similar than those *sp* grains that were not obviously in contact with melt. The compositions reported in Table 3 are averages of the *sp* grains that had similar compositions within each charge. As we discuss below, these mean compositions are consistent with the compositional trends of *sp* from other 9–12 kbar peridotite melting experiments.

Overall, although the pyroxenes and spinels in the experimental charges are not homogeneous within analytical error, our run durations were long compared with most previous peridotite melting experiments, and the observed heterogeneity is attributable to incompletely reacted cores that would be difficult to react fully without much finer starting materials or much longer experiments. As these cores do not make up a major fraction of the residual phases, it is unlikely that they have a significant influence on the results. More importantly, the compositional heterogeneities

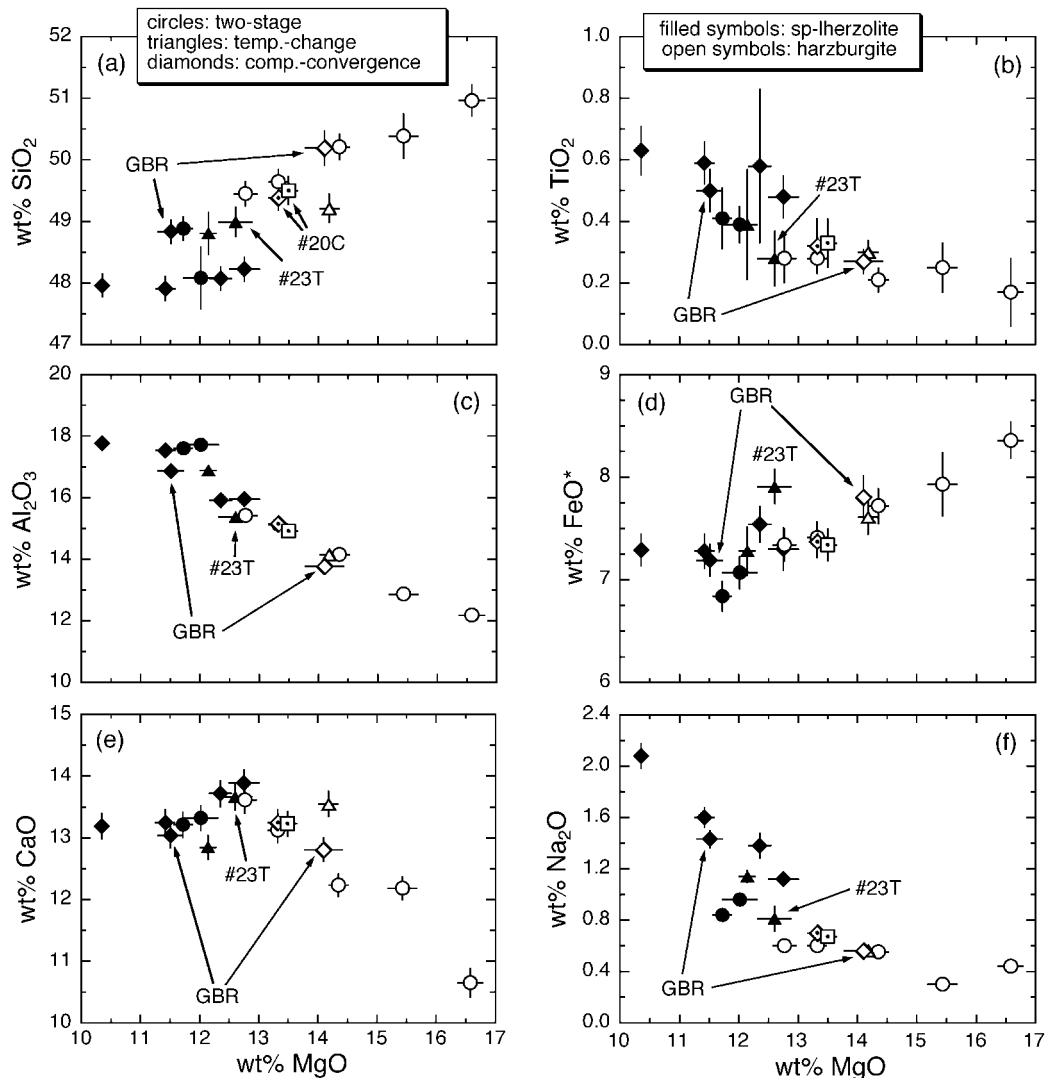


Fig. 4. Variation diagrams showing oxide concentrations in the experimental glasses as functions of MgO content. Circles represent glass compositions from the two-stage experiments; triangles represent glass compositions from the temperature-change runs; diamonds show the compositions of glasses from the 'compositional-convergence' experiments (see Tables 2 and 3). Glass compositions from the impregnated vitreous carbon chip (\diamond) and the separate vitreous carbon layer (\square) from run 20C are marked with small black circles. It should be noted that these two compositions overlap at the 1σ level in all six panels. The two 'compositional-convergence' experiments where the glass in the loaded vitreous carbon aggregate was Glass Buttes rhyolite are labeled GBR. Run 23T where the run temperature is inferred to have been $\sim 15^\circ\text{C}$ lower than the nominal temperature is also labeled. Error bars are 1σ ; if not shown, error bars are smaller than the symbols. Filled symbols represent glass coexisting with *ol*, *opx*, *cpx*, and *sp*; open symbols represent glass coexisting with *ol* and *opx*. MgO vs (a) SiO_2 , (b) TiO_2 , (c) Al_2O_3 , (d) FeO^* , (e) CaO , (f) Na_2O .

observed in pyroxenes and spinel within each charge do not appear to correlate with distance from the vitreous carbon aggregates.

Phase relations and liquid compositions

Our experiments span the $1250\text{--}1390^\circ\text{C}$ temperature range. Glass was present in all experiments run at $\geq 1270^\circ\text{C}$; no glass was detected in high-magnification,

backscattered electron images of the 1250°C experiment (36), and although such visual determinations can be misleading, we tentatively place the solidus for DMM1 between 1250 and 1270°C . Melt coexists with *ol*, *opx*, *cpx*, and *sp* at $1270\text{--}1300^\circ\text{C}$. Experiments at $1310\text{--}1390^\circ\text{C}$ contain liquid, *ol*, and *opx*, with the exception of experiment 23T (nominally 1325°C), which contains ~ 1 wt % of *cpx* at the end of the capsule far from the vitreous carbon aggregate and the thermocouple

junction. We interpret these results to indicate that *cp*x-out (the temperature at which *cp*x disappears from the solid residue) and *sp*-out are at 1300–1310°C. We attribute the *cp*x in run 23T to a deviation in nominal temperature at the limit of our stated $\pm 15^\circ\text{C}$ uncertainty, coupled with a temperature gradient along the length of the capsule. Comparison of the composition of glass in 23T with glasses from our other experiments (Fig. 4) shows that it is consistent with being just at *cp*x-out, and examination of compositional trends in 23T and the other experimental glasses with temperature (not shown) suggests that the temperature of run 23T was $\sim 1310^\circ\text{C}$.

Figure 4 shows the concentrations of selected oxides in glasses from our experiments as functions of MgO content. At constant pressure, the MgO content of peridotite partial melts is positively correlated with temperature (e.g. Hirose & Kushiro, 1993; Baker & Stolper, 1994; Walter, 1998; Falloon *et al.*, 1999), but our trends in glass composition are smoother when plotted against MgO content rather than temperature, presumably reflecting uncertainties in temperature in our experiments. Glass compositions from 1270 to 1390°C vary from basaltic (~ 11 –12 wt % MgO) at the low end of the temperature range to picritic (~ 17 wt % MgO) at the high end. Over this range of MgO contents, SiO₂, Cr₂O₃, and FeO* concentrations increase with increasing MgO, whereas TiO₂, Al₂O₃, and Na₂O abundances all decrease with increasing MgO. CaO contents display a more complex pattern, first increasing with increasing MgO content until *cp*x-out, after which the CaO content of melt decreases with increasing MgO content (and temperature). Except for SiO₂ and TiO₂, the trends displayed by the glasses are qualitatively similar to those observed in near-solidus melting experiments on fertile mantle compositions at 10 kbar (e.g. Hirose & Kushiro, 1993; Baker & Stolper, 1994; Baker *et al.*, 1995; Kushiro, 1996; Hirschmann *et al.*, 1998a). We will return to a more detailed comparison of 10 kbar depleted and fertile peridotite melting trends in the discussion section below.

Solid phase compositions

Olivine

The *mg*-number [defined as $100 \text{ MgO}/(\text{MgO} + \text{FeO}^*)$, molar] of *ol* in our experiments increases from ~ 89.8 at 1270–1275°C to 90.8 at 1390°C. $K_{\text{D,Fe}^*-\text{Mg}}^{\text{ol-liq}}$ values [$K_{\text{D,Fe}^*-\text{Mg}}^{\text{ol-liq}} = (\text{FeO}^{\text{ol}}/\text{FeO}^{\text{liq}})/(\text{MgO}^{\text{ol}}/\text{MgO}^{\text{liq}})$, where *liq* indicates liquid] are between ~ 0.28 and ~ 0.36 , with most values between 0.30 and 0.34. For comparison with our experimental results, we have compiled mineral and glass compositions from 142 experiments conducted at 9–12 kbar and 1200–1400°C that contain the residual solid phases

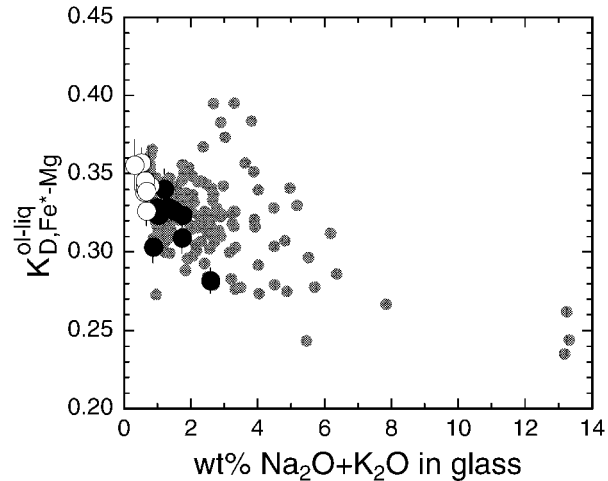


Fig. 5. Wt % Na₂O + K₂O in glasses coexisting with *ol* vs *ol*-*liq* $K_{\text{D,Fe}^*-\text{Mg}}$ values from DMM1 experiments. Large filled black circles represent *ol* + *opx* + *cp*x + *sp*-saturated experiments from this study; large open circles represent *ol* + *opx*-saturated experiments from this study. Vertical error bars were calculated by propagating analytical uncertainties on FeO and MgO in the *ol* and FeO* and MgO in the glass (Table 3; some vertical error bars are partially or completely masked by small gray circles); uncertainties on the sum of Na₂O + K₂O are smaller than the size of the symbols. Small filled gray circles are K_{D} values from 9–12 kbar experiments (1150–1400°C) from the literature (Takahashi & Kushiro, 1983; Falloon & Green, 1987; Ulmer, 1989; Kinzler & Grove, 1992a; Hirose & Kushiro, 1993; Baker & Stolper, 1994; Kushiro, 1996; Gaetani & Grove, 1998; Hirschmann *et al.*, 1998a; Wagner & Grove, 1998; Draper & Green, 1999; Falloon *et al.*, 1999, 2001; Pickering-Witter & Johnston, 2000; Schwab & Johnston, 2001; M. B. Baker, unpublished data, 1996).

ol + *opx* ± *cp*x ± *sp* ± plagioclase (Takahashi & Kushiro, 1983; Falloon & Green, 1987; Kinzler & Grove, 1992a; Hirose & Kushiro, 1993; Baker & Stolper, 1994; Kushiro, 1996; Gaetani & Grove, 1998; Hirschmann *et al.*, 1998a; Wagner & Grove, 1998; Falloon *et al.*, 1999, 2001; Pickering-Witter & Johnston, 2000; Schwab & Johnston, 2001; M. B. Baker, unpublished data, 1996). In Fig. 5 we plot our $K_{\text{D,Fe}^*-\text{Mg}}^{\text{ol-liq}}$ values and those from our literature dataset as a function of the alkali content of the coexisting glasses [this figure also includes the 10 kbar *ol*-*liq* $K_{\text{D,Fe}^*-\text{Mg}}$ values of Ulmer (1989) and Draper & Green (1999)]. Our dataset lies within and to the low-alkali end of the field defined by the literature values (Fig. 5). The decrease in $K_{\text{D,Fe}^*-\text{Mg}}^{\text{ol-liq}}$ with increasing alkalis in the melt in our data is also manifest in the main trend of the literature values (Fig. 5). The correlation between $K_{\text{D,Fe}^*-\text{Mg}}^{\text{ol-liq}}$ and alkalis is also seen in 1 atm experiments (e.g. Baker *et al.*, 1996) and reflects, in part, the effect of alkalis on increasing the Fe³⁺/Fe²⁺ ratio in silicate melts at constant temperature, pressure, and f_{O_2} (e.g. Sack *et al.*, 1980), although the Fe²⁺-Mg olivine-liquid exchange reaction also appears to be sensitive to bulk composition (e.g. Gee & Sack, 1988; Kushiro & Mysen, 2002).

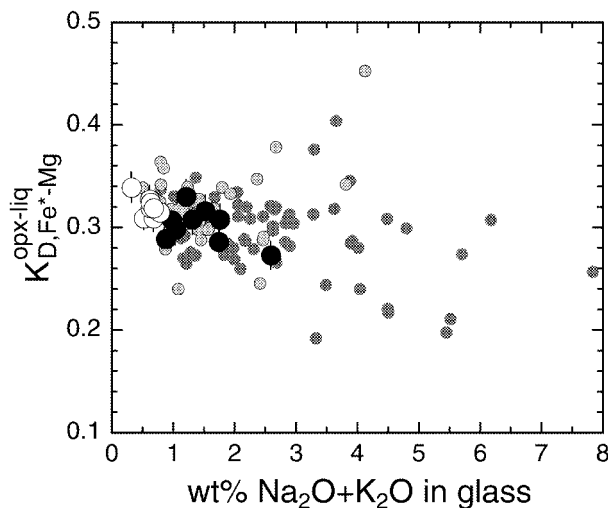


Fig. 6. Wt % Na₂O + K₂O in glasses coexisting with *opx* vs *opx*–*liq* $K_{D,Fe^{2+}-Mg}^{opx-liq}$ values from DMM1 experiments. Symbols as in Fig. 5, except for: small filled dark gray circles are K_D values from 9 to 12 kbar experiments where *opx* coexists with *ol* + *cpx* ± *sp* ± plagioclase (1225–1400°C); small filled light gray circles with black rims represent K_D values from *opx* coexisting with *ol* ± *sp* (1250–1400°C). Data sources listed in the caption to Fig. 5.

Orthopyroxene

With rising temperature, *opx* *mg*-numbers increase from 90.0–90.5 near the solidus (1270–1275°C) to ~91.5 at 1370–1390°C. Over this temperature range, $K_{D,Fe^{2+}-Mg}^{opx-liq}$ values increase with temperature from ~0.29 to ~0.32 and are also inversely correlated with Na₂O + K₂O in the coexisting glasses. Figure 6 shows that our $K_{D,Fe^{2+}-Mg}^{opx-liq}$ vs glass alkali trend is consistent with a large body of experimental data. $D_{Ca}^{opx/liq}$ values (CaO^{opx}/CaO^{liq}, both in wt %) from our experiments are consistent with values from other high-pressure experiments containing *opx* + *ol* ± *cpx*-saturated liquids. $D_{Ca}^{opx/liq}$ from our *cpx*-free runs show a slight decrease with rising temperature, but the mean values from the lherzolite- and harzburgite-saturated experiments are identical at 0.16 ± 0.02 (1 σ). These means also overlap with the mean $D_{Ca}^{opx/liq}$ values for *cpx*-bearing and *cpx*-free experiments from the literature (0.20 ± 0.04 and 0.16 ± 0.05 , 1 σ , respectively).

The *opx*–*liq* partition coefficient for Al₂O₃, $D_{Al}^{opx/liq}$, shows a weak negative correlation with temperature in our experiments, decreasing from 0.22–0.28 at 1270–1275°C to 0.15–0.23 at 1370–1390°C; the mean values from the *cpx*-bearing and *cpx*-free experiments overlap at the 1 σ level (0.24 ± 0.06 and 0.20 ± 0.03). $D_{Al}^{opx/liq}$ values from the literature show considerable scatter, with ranges of 0.14–0.51 (*cpx*-bearing) and 0.10–0.56 (*cpx*-free). The mean $D_{Al}^{opx/liq}$ values for the two sets of literature data (0.30 ± 0.09 and 0.25 ± 0.07 , 1 σ)

overlap with our lherzolite- and harzburgite-saturated experimental $D_{Al}^{opx/liq}$ values at the 1 σ level.

The *opx*–*liq* partition coefficients for Na₂O, $D_{Na}^{opx/liq}$, from our experiments are positively correlated with temperature: ranges of $D_{Na}^{opx/liq}$ values are 0.02–0.04 (0.028 ± 0.008 , 1 σ) for *cpx*-bearing assemblages and 0.03–0.07 (0.041 ± 0.012 , 1 σ) for *cpx*-free assemblages. However, the uncertainty on individual determinations is large (25–50%) because of the low concentration of Na₂O in the orthopyroxenes (0.02–0.05 wt %; Table 3). The mean $D_{Na}^{opx/liq}$ value for all 9–12 kbar experiments compiled from the literature is 0.04 ± 0.01 (1 σ), which overlaps with the mean values from our experiments (the literature mean includes all experiments containing glasses in the same range of Na₂O contents as our experiments, regardless of whether they contain *cpx*). The literature data also suggest a positive correlation with temperature, although again uncertainties on individual determination are large because of the low Na₂O contents of the *opx*.

$D_{Ti}^{opx/liq}$ values in our experiments are 0.03–0.20 (0.11 ± 0.05 , 1 σ) for *cpx*-bearing experiments and 0.07–0.18 (0.12 ± 0.04 , 1 σ) for *cpx*-free experiments and do not correlate with temperature. Again, individual $D_{Ti}^{opx/liq}$ values have large uncertainties (25–100%), as a result of the low concentrations of TiO₂ in the orthopyroxenes (0.01–0.08 wt %). Mean literature values from lherzolite- and harzburgite-saturated experiments are 0.20 ± 0.07 and 0.15 ± 0.08 (both 1 σ) and overlap with our results.

Clinopyroxene

$K_{D,Fe^{2+}-Mg}^{cpx-liq}$ values in our experiments are 0.29–0.36 with a mean of 0.32 ± 0.02 (1 σ). Figure 7a shows that these $K_{D,Fe^{2+}-Mg}^{cpx-liq}$ values are consistent with those from the literature and both sets of data display a weak inverse correlation with alkalis in the coexisting glass. Figure 7b compares $D_{Ca}^{cpx/liq}$ values from our experiments and from *cpx*–*liq* pairs saturated with *opx* from the literature with the weight percent sum of Na₂O and K₂O in the coexisting glasses. $D_{Ca}^{cpx/liq}$ values from the DMM1 *cpx*–*liq* pairs are consistent with the literature values; the positive correlation between $D_{Ca}^{cpx/liq}$ and Na₂O + K₂O reflects the effect of alkalis on the activity coefficient of calcium complexes in the melt (e.g. CaSiO₃; Hirschmann *et al.*, 1999a).

$D_{Al}^{cpx/liq}$ values from our experiments increase from ~0.28 at 1270°C to ~0.34 at 1300°C and fall in the field of literature values. Mean $D_{Al}^{cpx/liq}$ calculated for our data and for the compilation of literature data overlap at the 1 σ level (0.32 ± 0.03 for our DMM1 results vs 0.36 ± 0.08 for *cpx*–*liq* pairs from other peridotite melting experiments). $D_{Na}^{cpx/liq}$ values from our experiments and for the compilation of literature data

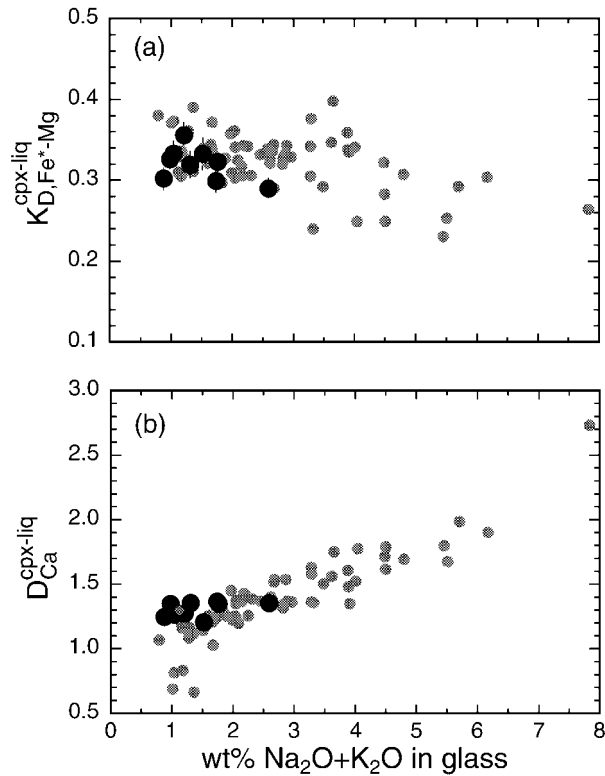


Fig. 7. Wt % Na₂O + K₂O in glasses coexisting with *cpx* vs (a) *cpx*-*liq* K_{D,Fe^*-Mg} values; (b) partitioning of CaO (wt %) between *cpx* and melt. Symbols as in Figs 5 and 6. Data sources listed in the caption to Fig. 5.

have identical means (0.16 ± 0.04 , 1σ). $D_{Na}^{cpx/liq}$ values do not correlate with temperature in either dataset. $D_{Ti}^{cpx/liq}$ values for the DMM1 experiments have large uncertainties (~ 25 – 75%), reflecting the low concentrations of titanium in the clinopyroxenes. The mean $D_{Ti}^{cpx/liq}$ value for our data is 0.22 ± 0.05 (1σ). This is lower than the mean of the literature values (0.38 ± 0.13 , 1σ), although there is considerable overlap between the two datasets. As discussed by Hirschmann *et al.* (1999a), at constant pressure $D_{Ti}^{cpx/liq}$ is positively correlated with the SiO₂ content of melt and negatively correlated with alkali content. The offset in $D_{Ti}^{cpx/liq}$ between the two sets of data thus plausibly reflects the generally lower SiO₂ and Na₂O + K₂O contents of the DMM1 glasses relative to the glasses in the 9–12 kbar literature compilation (47.8–48.9 vs 46.9–55.5 wt % SiO₂ and 0.8–2.1 vs 0.8–7.8 wt % Na₂O + K₂O, respectively).

Spinel

Although the spinel *mg*-number is a complex function of a number of variables, the most important are the *mg*-numbers of the coexisting phases, the partitioning of Al and Cr between *sp* and these phases, and the f_{O_2} .

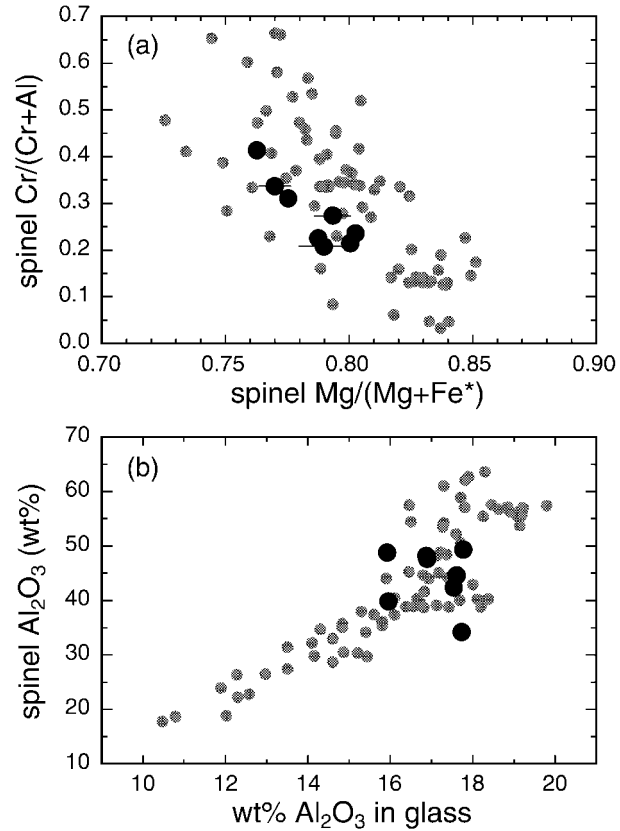


Fig. 8. (a) Cr/(Cr + Al) vs Mg/(Mg + Fe*) (molar) in spinel (Table 3). (b) Wt % Al₂O₃ in glasses vs Al₂O₃ (wt %) in the coexisting spinel (Table 3). In both panels, large filled black circles represent spinels and glasses from DMM1 experiments (this study). Error bars were calculated by propagating analytical uncertainties associated with FeO*, MgO, Cr₂O₃, and Al₂O₃ in *sp*, or plotting the 1σ values associated with the Al₂O₃ contents in *sp* and coexisting glasses; where not visible they are smaller than the size of the symbols. Small filled gray circles are spinels [with Cr/(Cr + Al) ≥ 0.03] and coexisting glasses from 9–12 kbar experiments from the literature (Falloon & Green, 1987; Baker & Stolper, 1994; Hirschmann *et al.*, 1998a; Gaetani & Grove, 1998; Falloon *et al.*, 1999, 2001; Pickering-Witter & Johnston, 2000; Schwab & Johnston, 2001; M. B. Baker, unpublished data, 1996).

Figure 8a shows that the mean *sp* compositions in our experiments overlap the inverse correlation between *mg*-number and *cr*-number [$100Cr/(Cr + Al)$, molar] displayed by spinels from other 9–12 kbar peridotite melting studies. In addition, the Al₂O₃ contents of *sp* and coexisting liquid in our experiments (Fig. 8b) are consistent with the trend of data from other 9–12 kbar experiments.

DISCUSSION

Melting reactions and melt productivity

Proportions of glass and crystalline phases in each experiment were calculated by mass balance using an

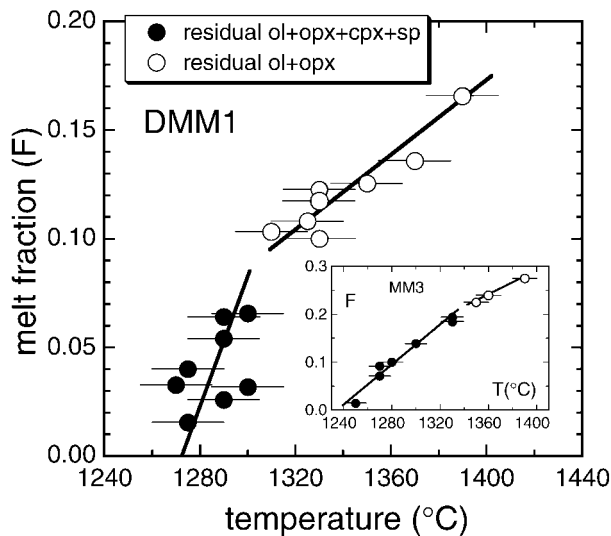


Fig. 9. Temperature ($^{\circ}\text{C}$) vs melt fraction (F) for experiments on DMM1. Because of its uncertain temperature, run 23T is not plotted (see text). Results for experiments on MM3 are shown in the insert (Baker & Stolper, 1994; Hirschmann *et al.*, 1998a; M. B. Baker, unpublished data, 1996). Filled black circles are runs with a spinel lherzolite residual assemblage (plus *sp* in the case of MM3). Open circles are runs with a harzburgite residual assemblage. Melt fractions were calculated by mass balance using the compositions of glass and coexisting phases in each experiment and the bulk composition (for DMM1, data used in the mass balance are listed in Tables 1 and 3; mass balance results are given in Table 2). All oxide values in each mass balance were weighted by their respective uncertainties (Albarède & Provost, 1977). Temperature uncertainties are $\pm 15^{\circ}\text{C}$ for the DMM1 experiments and $\pm 10^{\circ}\text{C}$ for the MM3 experiments. In both panels, uncertainties on the best-fit melt fractions are smaller than the size of the symbols. Continuous lines are weighted least-squares fits to the data using errors on both T and F . Equations for DMM1: $-3.80(2.91) + 0.0030(22)T(^{\circ}\text{C}) = F$ (spinel lherzolite field); $-1.03(19) + 0.00086(14)T(^{\circ}\text{C}) = F$ (harzburgite field). Equations for MM3: $-2.58(23) + 0.0021(2)T(^{\circ}\text{C}) = F$ (spinel lherzolite field); $-1.44(7) + 0.0012(1)T(^{\circ}\text{C}) = F$ (spinel harzburgite field). Values in parentheses are standard deviations on the y -intercepts and slopes, respectively, in terms of the least units cited.

algorithm that incorporates uncertainties in both the bulk composition and the compositions of the coexisting phases (Albarède & Provost, 1977). Liquid fractions increase from ~ 0.02 – 0.04 at 1270 – 1275°C to ~ 0.17 at 1390°C (Fig. 9). A weighted linear fit of melt fraction (F) vs temperature (T), using errors on both F (Table 2) and T ($\pm 15^{\circ}\text{C}$; Reed, 1992), of the spinel lherzolite-saturated glasses yields a solidus temperature of $1272 \pm 11^{\circ}\text{C}$ (1σ), within our experimental bracket of 1250 – 1270°C (because of its uncertain temperature, run 23T was not included in the fit). Weight fractions of *ol* and *opx* change from ~ 0.64 and ~ 0.27 at 1270°C to 0.69 and ~ 0.19 at 1390°C . Weight fractions of *cpx* and *sp* decrease from ~ 0.06 and 0.005 at the solidus to 0 at 1300 – 1310°C .

Figure 10 shows the fractions of residual solid phases plotted against melt fraction. The lines are weighted

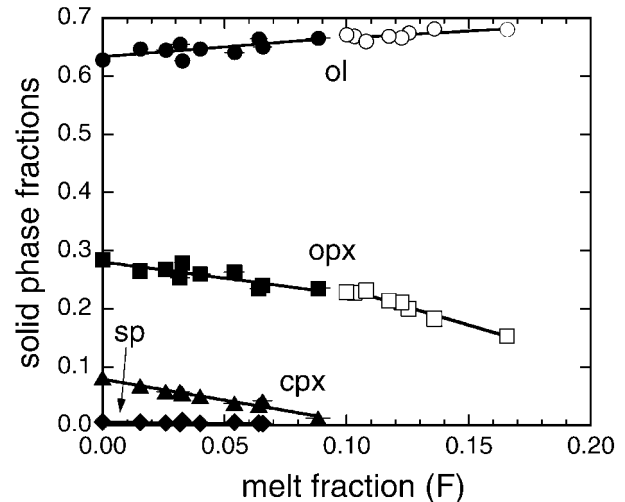


Fig. 10. Weight fractions of residual crystalline phases as functions of the weight fraction of glass in experiments from this study. For each experiment, the weight fraction of all phases (crystals and glass) equals 1.0 (see Table 2). Filled symbols represent spinel lherzolite residual assemblages; open symbols represent harzburgite residual assemblages. Circles are *ol*, squares are *opx*, triangles are *cpx*, diamonds are *sp*. Error bars on all phases are 1σ and are smaller than the symbol sizes for many experiments. The continuous lines are weighted, linear, least-squares fits to the phase proportions in the supersolidus and subsolidus experiments (F was set to zero in the subsolidus run, 36; only errors on the solid phases were used in the fits). For the spinel lherzolite assemblages, the equations of the fits are: $ol = 0.634(5) + 0.34(10)F$; $opx = 0.281(5) - 0.56(10)F$; $cpx = 0.079(2) - 0.72(4)F$; $sp = 0.0056(6) - 0.039(14)F$. Equations in the residual harzburgite field are: $ol = 0.642(16) + 0.24(13)F$; $opx = 0.358(18) - 1.24(14)F$. Values in parentheses are standard deviations on the y -intercept and slope, respectively, in term of the least units cited; e.g. $0.634(5) = 0.634 \pm 0.005$.

least-squares fits to the *ol* + *opx* + *cpx* + *sp*-saturated and *ol* + *opx*-saturated melts, respectively. As discussed by Baker & Stolper (1994), multiplying the slopes of these lines by -1 yields the melting reaction coefficients. In the spinel lherzolite field, the resulting equation is

$$0.56(10)opx + 0.72(4)cpx + 0.04(1)sp \\ = 0.34(10)ol + liq.$$

These coefficients are compared with those based on 10 kbar data on the melting of spinel lherzolite assemblages in the literature in Table 4. The reaction relationship between *ol* and liquid indicated by our data for DMM1 is a robust result from all studies of spinel lherzolites. As noted by Kinzler & Grove (1992a), Baker & Stolper (1994), and Pickering-Witter & Johnston (2000), *cpx* reaction coefficients show little variation over a wide range of multi-component spinel lherzolite compositions (the total range is 0.72 – 0.82) and dominate each melting assemblage. However, as illustrated by Table 4, the values of the reaction coefficients for *ol* and *opx* are

Table 4: 10 kbar spinel lherzolite and spinel harzburgite and harzburgite melting reaction coefficients

	orthopyroxene	clinopyroxene	spinel	olivine	range of F^*	Na ₂ O + K ₂ O [†]	cpx mode [‡]
DMM1	0.56(10)	0.72(4)	0.04(1)	0.34(10)	0.02–0.09	1.3(5)	0.079(2)
MM3	0.38(6)	0.77(3)	0.063(6)	0.21(4)	0.01–0.19	3.4(2.0)	0.181(4)
FER-E	0.27(8)	0.78(5)	0.057(6)	0.10(5)	0.05–0.30	2.3(9)	0.29(1)
K&G 92a	0.40	0.82	0.08	0.30			
DF80	0.40	0.82	0.15	0.38	0.03–0.18	0	0.19
DMM1	1.24(14)			0.24(13)	0.10–0.17	0.56(9)	
MM3	1.06(36)		0.04(3)	0.10(30)	0.22–0.27	1.25(8)	
FER-C	0.88(16)		0.24(2)	0.12(13)	0.02–0.12	1.6(9)	
FER-D	1.09(10)		0.20(1)	0.29(8)	0.15–0.30	1.1(3)	
INT-D	1.31(11)		0.15(1)	0.46(8)	0.17–0.41	0.51(12)	

Data sources: DMM1: this study (experimental modes listed in Table 2, runs 23T and 36 were included in the spinel lherzolite fit, for 36 F was set to zero); MM3: Baker & Stolper (1994), Hirschmann *et al.* (1998a), M. B. Baker (unpublished data, 1996); FER-E, FER-C, FER-D: Pickering-Witter & Johnston (2000), run FER-C5 was not included in the fits for FER-C because of the high *ol-liq* K_D value (0.49) in this run; K&G 92a: Kinzler & Grove (1992a); DF80: Gudmundsson & Presnall (2000); INT-D: Schwab & Johnston (2001). All except K&G 92a are specific peridotite bulk compositions; K&G 92a references melting reaction coefficients listed in fig. 2 of Kinzler & Grove (1992a) that were extracted from the results of 10 kbar peridotite melting experiments of Falloon & Green (1987). The coefficients for DF80 were calculated from mass balance results using the phase parameterizations of Gudmundsson & Presnall (2000) in the system CaO–MgO–Al₂O₃–SiO₂–FeO; the spinel lherzolite melting reaction is metastable at 10 kbar. Coefficients for the remaining compositions are based on at least three experiments with the same phase assemblage and represent the slopes of weighted least-squares fits to F vs each solid phase (using errors on the solid phases).

*Range of melt fractions (F , rounded to the nearest 0.01) in the experiments that were used to fit the melting reaction for each bulk composition (in either the spinel lherzolite or harzburgite \pm spinel fields). Kinzler & Grove (1992a) did not specify which experiments of Falloon & Green (1987) were used, and thus no range of F values, Na₂O + K₂O value, or cpx mode is listed. [†]Na₂O + K₂O values are the mean concentrations and 1 σ values (in parentheses) in the experimental glasses over the range of melt fractions used to fit the melting reactions. The equation Na₂O + K₂O = $C_o/[F + D(1 - F)]$ was used to fit the Na₂O + K₂O concentrations in all glasses of a given bulk composition as a function of F (with C_o and D as fit parameters); then Na₂O + K₂O values were calculated for the range of F values in increments of 0.01 for each set of melting reaction coefficients (see above); finally, the calculated alkali values for each set of coefficients were averaged.

variable (0.10–0.38 and 0.27–0.56, respectively). There is a crude inverse correlation between the mean alkali content in the glasses used in the fits for each bulk composition's reaction coefficients and the *opx* and *ol* melting coefficients.

At temperatures above *cpx* + *sp*-out, the reaction for melting of DMM1 is based on the best-fit lines in Fig. 10 and is

$$1.24(14)opx = 0.24(13)ol + 1liq.$$

Harzburgite \pm spinel melting reaction coefficients at 10 kbar for other bulk compositions are listed for comparison in Table 4. Although all the melting reactions listed in Table 4 above *cpx*-out have olivine in reaction relation, the reaction coefficients for all three solid phases (0.88–1.3 for *opx*; 0.1–0.46 for *ol*; 0.04–0.24 for *sp*) are highly variable; again, there is a crude inverse correlation between alkali content in the glasses and the *opx* and *ol* melting reaction coefficients.

Isobaric melt productivity, $(\partial F/\partial T)_P$, is an important term in the equation describing melt production during adiabatic mantle upwelling (e.g. Asimow *et al.*, 1997). By analogy with simple systems and based on MELTS (Ghiorso & Sack, 1995) calculations on peridotite compositions (including DMM1 and MM3), we expect a steady increase in $(\partial F/\partial T)_P$ up to *cpx*-out (Hirschmann *et al.*, 1999b). At *cpx*-out, a discontinuous drop in productivity is expected, and the T vs F trend is expected to remain concave-up with further rises in temperature (Asimow *et al.*, 1997; Hirschmann *et al.*, 1999b). To determine average values for $(\partial F/\partial T)_P$ for *ol* + *opx* + *cpx* + *sp*-saturated and *ol* + *opx*-saturated melting of the DMM1 composition, we fitted our $T(^{\circ}\text{C})$ vs F data (Table 2 and Fig. 9; excluding run 23T) to straight lines below and above *cpx*-out. The best-fit average melt productivities are $0.3 \pm 0.2\%/^{\circ}\text{C}$ (1 σ) for *cpx*-saturated melting and $0.08 \pm 0.01\%/^{\circ}\text{C}$ (1 σ) above *cpx*-out. For comparison, the fertile MM3 peridotite composition has best-fit productivities of

$0.21 \pm 0.02\%/^{\circ}\text{C}$ (1σ) for *cpx*-saturated melting and $0.12 \pm 0.01\%/^{\circ}\text{C}$ (1σ) above *cpx*-out (Baker & Stolper, 1994; Hirschmann *et al.*, 1998a; M. B. Baker, unpublished data, 1996).

Both the DMM1 and MM3 compositions show the expected discontinuous drop in productivity associated with the exhaustion of *cpx* (Asimow *et al.*, 1997). However, given the large uncertainties associated with the isobaric melt productivity of DMM1, we cannot evaluate whether $(\partial F/\partial T)_P$ for DMM1 near the solidus is larger than that of MM3 (for identical low values of F where both compositions have the same residual phase assemblage), as expected based on the calculations of Hirschmann *et al.* (1999b). Moreover, the T - F data for DMM1 in the spinel lherzolite field (Fig. 9) are not adequate to constrain whether $(\partial F/\partial T)_P$ is constant or dependent on F , as expected from analysis of simple systems and MELTS calculations (Asimow *et al.*, 1997; Hirschmann *et al.*, 1999b). However, for MM3 the T - F data in the spinel lherzolite field cannot be fitted with a concave-upward curve (Fig. 9 inset) and the 15 kbar peridotite melting experiments of Robinson *et al.* (1998) also yield nearly constant melt productivities in the spinel lherzolite field. In contrast, 10 kbar experiments on the FER-E and INT-E compositions (Pickering-Witter & Johnston, 2000; Schwab & Johnston, 2001) suggest that melt productivities do indeed increase with rising temperature in the spinel lherzolite field. We do not have an explanation for the diversity of isobaric productivity functions that have been observed experimentally for lherzolite melting.

The effects of peridotite composition on 10 kbar near-solidus partial melts

Partial melts generated from depleted peridotite differ in several important ways from partial melts of fertile peridotite. Figure 11 illustrates some of these differences by comparing liquid compositions from this study as functions of melt fraction with trends of 10 kbar partial melt compositions from experiments on fertile peridotites. We have included the glass data of MM3 (Baker & Stolper, 1994; Baker *et al.*, 1995; Hirschmann *et al.*, 1998a; M. B. Baker, unpublished data, 1996), KLB-1 (Hirose & Kushiro, 1993), PHN1611 (Kushiro, 1996), and FER-E (Pickering-Witter & Johnston, 2000).

At melt fractions of 0.1–0.2, SiO_2 contents of the DMM1 experimental glasses overlap those of experimental glasses from the fertile peridotite compositions (Fig. 11a). At lower melt fractions, however, partial melts of all the fertile peridotites display increases in their silica contents, whereas the silica contents of the DMM1 partial melts continue to decrease with

decreasing F . This difference in the behavior of SiO_2 in near-solidus melts of fertile and depleted peridotite reflects the effects of alkalis on the liquid silica activity coefficient [at 1 atm, these effects have been discussed by Kushiro (1975) and Ryerson (1985)]. As emphasized by Hirschmann *et al.* (1998a), the silica activity of *opx* + *ol*-saturated liquids varies little with melt fraction, but the activity coefficient of silica in the liquids decreases significantly with increasing alkali content. Consequently, as Na_2O + K_2O concentrations of liquids increase to high levels with decreasing F in melting experiments on fertile lherzolites, the SiO_2 concentrations likewise increase. However, the alkali contents of glasses in the DMM1 experiments are low relative to partial melts of more fertile peridotite, and the effects of increasing alkali contents on the SiO_2 contents of partial melts would only be expected to be expressed at very low melt fractions. For example, Fig. 11e shows that at $F \sim 0.02$, the Na_2O concentration in the DMM1 melt is only ~ 2 wt %, much lower than partial melts of more fertile peridotites such as MM3, where at $F \sim 0.02$ the Na_2O contents can reach concentrations > 7 wt %. It should be noted also that the SiO_2 contents of the partial melts of the fertile peridotites begin to increase only when Na_2O contents reach ~ 3 wt %. Thus the lack of increasing SiO_2 contents in the DMM1 glasses at melt fractions down to ~ 0.02 (where Na_2O content is only ~ 2 wt %) is consistent with the results from fertile peridotites. MELTS calculations predict that for the DMM1 composition alkali contents build up sufficiently to cause increases in silica contents only at melt fractions lower than ~ 1 wt % (Hirschmann *et al.*, 1998b).

Although we have emphasized the role of Na_2O , which is the most abundant alkaline component, concentrations of K_2O in the melts of fertile peridotite are also important: at $F \sim 0.02$, the 10 kbar partial melt of MM3 contains ~ 0.43 wt % K_2O (Hirschmann *et al.*, 1998a); at $F \sim 0.04$, the 10 kbar partial melt of PHN1611 contains 3.2 wt % K_2O (Kushiro, 1996). Overall, such high values of Na_2O + K_2O can lead to significant changes in melt chemistry in addition to increasing SiO_2 contents (Fig. 11a), such as less incompatible behavior of Ti and other highly charged incompatible trace elements (e.g. U^{4+} , Th^{4+} , Ta^{5+} , Hf^{4+}) in *cpx* and decreasing *ol*-*liq*, *opx*-*liq*, and *cpx*-*liq* $K_{D,\text{Fe}^*\text{-Mg}}^{\text{ol-liq}}$ values (e.g. Baker *et al.*, 1995; Hirschmann *et al.*, 1998a, 1999a; see Figs 5, 6, and 7). The deviation in the F vs FeO^* trend of DMM1 partial melts relative to the trends of melts of fertile peridotites at low F (Fig. 11c) also reflects the low alkali contents in the near-solidus melts of DMM1 relative to those of fertile peridotites. At constant melt fraction a decrease in the alkali content in an *ol* + *opx*-saturated liquid decreases the stability of *ol* (the most Fe-rich silicate phase) relative to *opx*

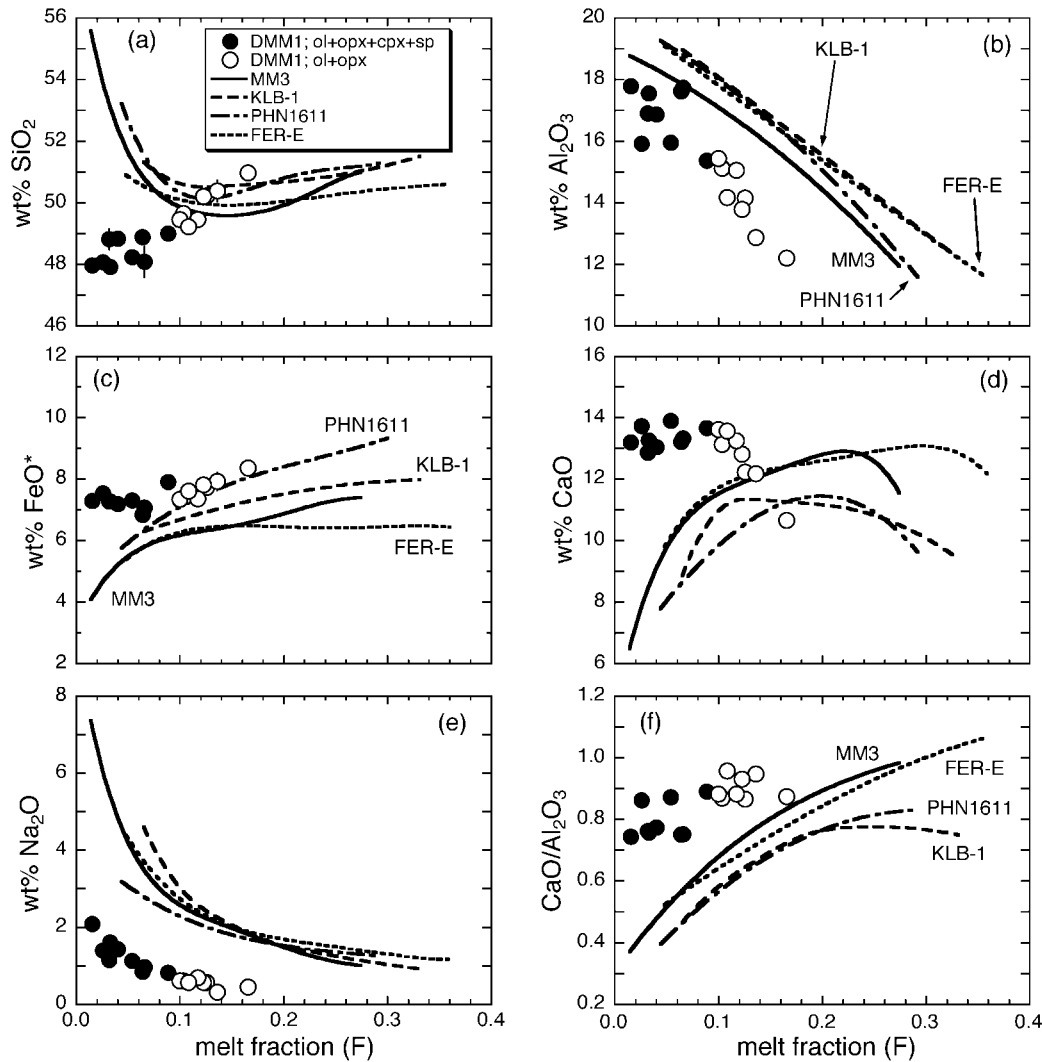


Fig. 11. Melt fraction vs glass composition from the DMM1 experiments (this study) compared with trends from experimental studies on fertile mantle compositions. All experiments were conducted at a nominal pressure of 10 kbar. ●, DMM1 glasses coexisting with *ol + opx + cpx + sp*; ○, DMM1 glasses coexisting with only *ol + opx*; oxide error bars and melt fraction uncertainties are all 1σ (and in many cases are smaller than the size of the symbols). The melting trends for the fertile peridotite compositions are represented by curves fitted to the data points of each study using either a polynomial or a Stineman function (Stineman, 1980). Continuous curve: MM3 (Baker & Stolper, 1994; Baker *et al.*, 1995; Hirschmann *et al.*, 1998a; M. B. Baker, unpublished data, 1996); long-dash curve: KLB-1 (Hirose & Kushiro, 1993); dot-dash curve: PHN1611 (Kushiro, 1996); short-dash curve: FER-E (Pickering-Witter & Johnston, 2000). Melt fraction vs (a) SiO_2 , (b) Al_2O_3 , (c) FeO^* , (d) CaO , (e) Na_2O , (f) $\text{CaO}/\text{Al}_2\text{O}_3$. All oxide concentrations are in wt %.

(Kushiro, 1975), which in turn increases the FeO^* content in the melt.

Alumina contents of partial melts from the five peridotite compositions plotted in Fig. 11b decrease with increasing melt fraction, but partial melts of DMM1 contain $\sim 2\text{--}4$ wt % less Al_2O_3 than melts from the more fertile bulk compositions, with the deviation increasing slightly with increasing F . The lower Al_2O_3 contents in the partial melts of DMM1 compared with those of the fertile peridotites at all melt fractions probably reflect several different factors, including the 18–80% lower alumina content of

DMM1 relative to the fertile peridotites and the effect of alkali content on the activity coefficient of Al_2O_3 in peridotite melts (Hirschmann *et al.*, 1999a).

For DMM1, CaO contents in *cpx*-saturated liquids increase from ~ 13 to nearly 14 wt % with increasing melt fraction and then decrease with increasing F beyond the exhaustion of *cpx* (Fig. 11d). In contrast, the CaO contents of *cpx*-saturated partial melts of the fertile peridotites increase by up to a factor of two with increasing melt fraction from $F \sim 0.02$ up to the point of *cpx* exhaustion, after which the CaO contents of the partial melts decrease rapidly with further melting. For

DMM1 and the fertile peridotites, the maximum CaO contents occur at different melt fractions (0.09–0.10 for DMM1, 0.10–0.30 for the fertile peridotites); this is because the maximum CaO content occurs at the exhaustion of *cpx* from the solid residue, which occurs at different values of F for peridotites with different initial *cpx* contents. An important result is that the maximum CaO contents in the DMM1 partial melts are 1–2.5 wt % higher than the maximum values of melts from the more fertile compositions even though the DMM1 bulk composition has ~1–3 wt % less CaO than the more fertile mantle compositions. The elevated CaO contents of melts of the depleted DMM1 composition relative to partial melts of the fertile compositions are even more dramatic at low F ; for example, at $F \sim 0.02$, partial melts of DMM1 contain ~13 wt % CaO compared with ~6.5 wt % for partial melts of MM3. The explanation for this significant difference again lies in the much higher alkali contents of near-solidus melts of fertile peridotite relative to melts of DMM1 (Hirschmann *et al.*, 1999a). The alkali-rich partial melts of the fertile peridotites have higher CaO activity coefficients relative to alkali-poor melts of depleted lherzolite. The higher CaO activity coefficients in turn result in lower concentrations of CaO in alkali-rich, *cpx*-saturated liquids compared with alkali-poor, *cpx*-saturated liquids, as the activity of CaO is roughly fixed in lherzolite-saturated melts (Hirschmann *et al.*, 1999a). It should be noted that the difference in CaO contents of *cpx*-saturated melts of fertile and depleted peridotites, first discussed quantitatively by Hirschmann *et al.* (1999a), is somewhat unintuitive. The fertile peridotites, although richer in CaO, generate partial melts that are poorer in CaO, and experimental confirmation of this phenomenon is an important result of this study.

CaO/Al₂O₃ ratios in partial melts of DMM1 and four fertile peridotite compositions are plotted in Fig. 11f. These ratios lie in a narrow band for the melts of fertile peridotite, increasing from ~0.4 to 0.7 as F increases from 0.02 to 0.15. This simple trend has led to the use of CaO/Al₂O₃ in primitive MORBs as a proxy for the extent of melting (e.g. Niu & Batiza, 1991; Niu & Hékinian, 1997). However, for melts of depleted peridotites, the CaO/Al₂O₃ ratios of low-degree partial melts of DMM1 are as high as those of high-degree melts of fertile peridotite and increase slowly with increasing F (Fig. 11f; Hirschmann *et al.*, 1999a). The high CaO/Al₂O₃ ratios and their small range in the DMM1 melts reflect primarily the low degree of variation in CaO contents before *cpx* exhaustion compared with CaO in partial melts of fertile peridotite; above *cpx*-out, CaO and Al₂O₃ trends generally have similar slopes and thus less variation in CaO/Al₂O₃ ratios (Fig. 11b and d). The key point of

Fig. 11f, as anticipated by Hirschmann *et al.* (1999a), is that variations of CaO/Al₂O₃ with F in partial melts depend strongly on source peridotite composition; thus CaO/Al₂O₃ must be used cautiously as an indicator of degree of partial melting in a series of basalts.

Comparison of experiments and mantle melting models

A wide range of models have been developed for calculating the compositions of partial melts of peridotite under upper-mantle conditions (e.g. McKenzie & Bickle, 1988; Niu & Batiza, 1991; Kinzler & Grove, 1992a, 1992b; Langmuir *et al.*, 1992; Ghiorso & Sack, 1995; Kinzler, 1997; Ghiorso *et al.*, 2002; Longhi, 2002). Most high-pressure experiments that have been available to calibrate these models have come from melting of fertile peridotites and pyroxene-enriched compositions, so the degree to which they can model the melting behavior of more depleted compositions is uncertain. Yet, as emphasized in the Introduction, current thinking about the dynamics of partial melting processes suggests that melt extraction occurs throughout the melting process, producing variously depleted peridotite compositions in much of the MORB source region. Therefore accurate modeling of MORB generation must handle well the melting behavior of depleted peridotitic compositions. Our experimental results provide an opportunity to evaluate the performance of these models on a depleted peridotite composition far removed from the data used to calibrate them.

Figure 12 shows melt fractions vs major element concentrations for the experimental glasses presented in this paper and compares them with the results of calculations on the DMM1 bulk composition using four of the available models of peridotite melting. Calculations are shown for the thermodynamically based MELTS (Ghiorso & Sack, 1995) and pMELTS (Ghiorso *et al.*, 2002) algorithms. pMELTS is a better calibrated version of the MELTS model, based on a much larger high-pressure experimental dataset for calculating crystal–liquid equilibria in silicate systems by thermodynamic potential minimization. pMELTS also incorporates a revised thermodynamic model and equation of state for the silicate melt. Also shown in Fig. 12 are liquids calculated using BATCH (Longhi, 2002), based on parameterizations of multiply saturated phase boundaries and mineral–melt distribution coefficients, and the expressions of Langmuir *et al.* (1992), based on selected mineral–melt distribution coefficients parameterized using T , pressure (P), and liquid compositions. It should be noted that the expressions of Langmuir *et al.* (1992) cannot calculate liquid SiO₂, Al₂O₃, or CaO contents.

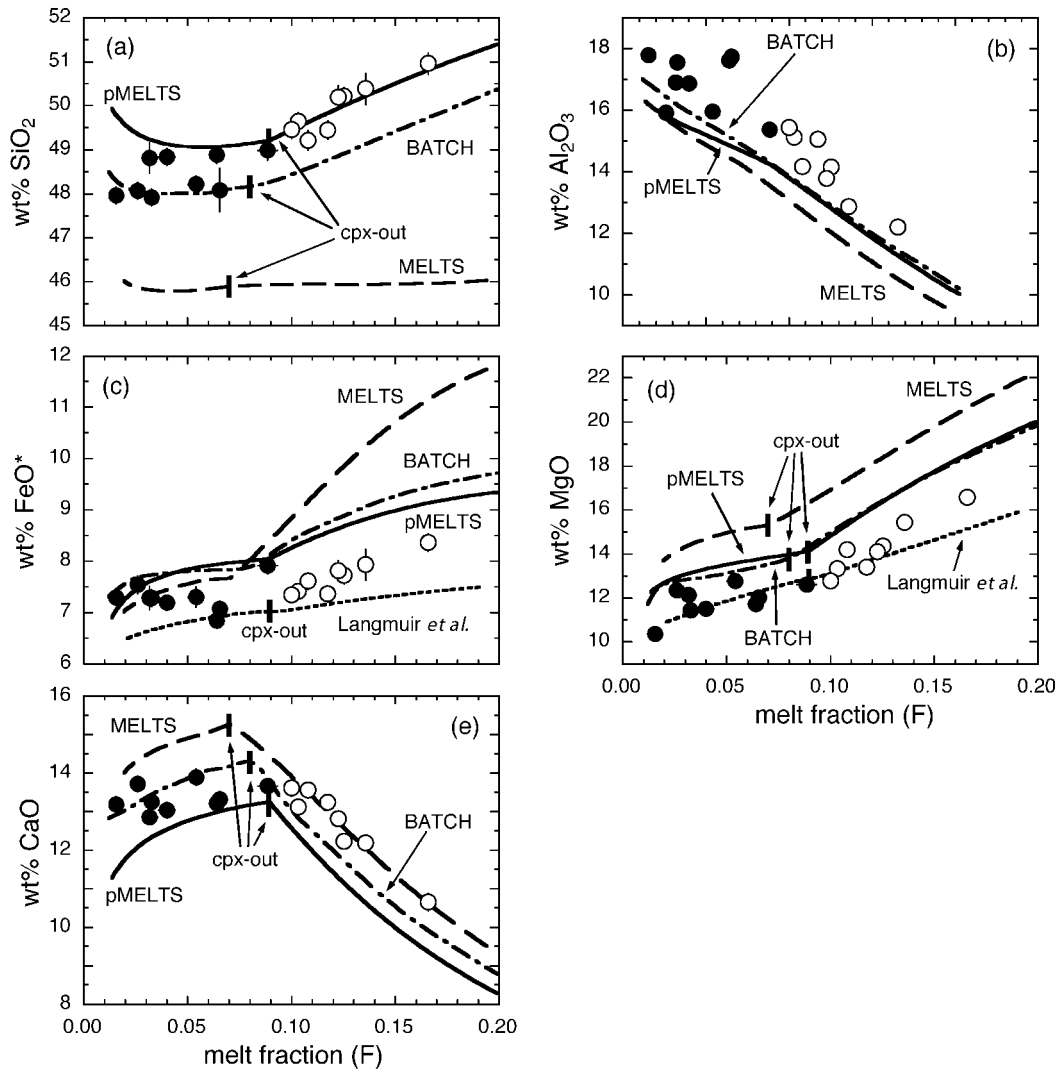


Fig. 12. Comparison of experimental glass compositions (● and ○, this study) as functions of melt fraction from melting experiments on DMM1 with partial melts calculated for the DMM1 bulk composition using several different melting models: pMELTS (Ghiorso *et al.*, 2002; continuous curve); MELTS (Ghiorso & Sack, 1995; long-dash curve); BATCH (Longhi, 2002; dot-dash curve); and the expressions of Langmuir *et al.* (1992; short-dash curve). All calculations are for 10 kbar. In the pMELTS and MELTS calculations, f_{O_2} was set at QFM - 2; calculations were also carried out at QFM, but those at QFM - 2 more closely match the F vs FeO^* and F vs MgO trends of the experimental glasses. ●, glasses coexisting with $ol + opx + cpx + sp$; ○, glasses coexisting with only $ol + opx$. Oxide error bars as in Fig. 4. Melt fraction values and uncertainties for the experimental glasses are from mass balance calculations (see Table 2); for the calculated melting paths, the melt fractions are those output by each program. A short, thick, vertical line on the calculated trends denotes *cpx-out* (not shown in all panels). The Langmuir *et al.* (1992) expressions do not calculate SiO_2 , Al_2O_3 , or CaO liquid contents. Melt fraction vs (a) SiO_2 , (b) Al_2O_3 , (c) FeO^* , (d) MgO , (e) CaO , all in wt %.

The four models shown in Fig. 12 were chosen because they could handle the DMM1 composition with either little [the expressions of Langmuir *et al.* (1992)] or no modification (MELTS, pMELTS, BATCH). Although we show the MELTS trends in Fig. 12 for completeness, we concentrate on the comparison between the calculated pMELTS liquids and DMM1 glass compositions because the MELTS–DMM1 comparison was discussed by Hirschmann *et al.* (1998b). The calculations for the Langmuir

et al. model were performed using a spreadsheet provided by C. H. Langmuir (personal communication, 1998). In using this spreadsheet, we adjusted the variable that controls the relationship between temperature and melt fraction so as to match the experimental solidus temperature of DMM1. We also entered the modal abundance of *cpx* for DMM1 at its solidus (from the intercept at $F = 0$ of the linear fit to *cpx* abundance shown in Fig. 10) and changed the *cpx* melting reaction coefficient in the spreadsheet so as

to reproduce the trend of F vs cpx abundance shown by our results in Fig. 10.

For SiO_2 (Fig. 12a) above cpx -out, the liquids calculated with pMELTS match the glasses produced by melting DMM1. Although those liquids calculated with BATCH have the correct slope, they are on average ~ 1 wt % too low. Below cpx -out, both calculated trends have approximately constant liquid SiO_2 contents for $F \geq \sim 0.02$, but the pMELTS-calculated liquids are on average ~ 0.8 wt % too high in SiO_2 , and the BATCH-calculated liquids are on average ~ 0.3 wt % too low. The pMELTS trend shows a slight upturn in liquid SiO_2 content at the lowest calculated melt fractions; as described above, this effect reflects the elevation in alkalis at very low melt fractions. It should be noted that the pMELTS-calculated occurrence of cpx -out at $F \sim 0.09$ corresponds well to the occurrence of cpx -out in our experiments ($F \sim 0.09$ – 0.10), indicating that pMELTS is successful at reproducing a key aspect of the melting behavior. For BATCH, cpx -out occurs at $F \sim 0.08$. MELTS-calculated liquids are displaced to significantly lower silica contents than the experimental data; this inaccuracy in MELTS is well known and reflects the overstability of opx and understability of ol for peridotite compositions (e.g. Hirschmann *et al.*, 1998b; Ghiorso *et al.*, 2002).

Al_2O_3 contents of partial melts of DMM1 calculated using MELTS, pMELTS, and BATCH are all displaced downwards, but are parallel to the experimental data (Fig. 12b). Mean absolute deviations between the experimental glass compositions and the liquid compositions calculated using pMELTS and BATCH are 1.37 and 1.16 wt % Al_2O_3 , respectively. For pMELTS, the main cause of this systematic deviation is the 3.5–4.5 times higher sp contents in the calculated near-solidus residues compared with the experimental modes, and the fact that above cpx -out, sp is still a residual phase in the pMELTS calculations over the range of F values plotted in Fig. 12 (recall that sp - and cpx -out occur over the same melting interval in our experiments). The systematic deviations in liquid Al_2O_3 contents in the BATCH calculations reflect (at the same melt fractions) the higher Al_2O_3 contents in the calculated cpx and opx compared with the Al_2O_3 contents in the our experimental pyroxenes. Although F vs liquid Al_2O_3 contents from both models show systematic deviations from the experimental data, both models predict the approximately linear decrease in liquid Al_2O_3 content with increasing melt fraction (Fig. 12b).

At the same melt fraction, FeO^* and MgO contents of DMM1 partial melts calculated using pMELTS and BATCH are similar, but their F vs FeO^* and MgO trends plot above, but parallel to, the experimental glass compositions (Fig. 12c and d). The mean absolute deviations are 0.67 wt % FeO^* and 1.65 wt % MgO

for the pMELTS-calculated trends and 0.76 wt % FeO^* and 1.55 wt % MgO for the BATCH-calculated trends. Both models reproduce the slope changes in F vs FeO^* and MgO at cpx -out. The Langmuir *et al.* model predicts liquids with lower FeO^* and similar MgO contents to the experimental glasses. The mean absolute deviations in FeO^* and MgO are 0.52 and 0.35 wt %, respectively. In contrast to the pMELTS and BATCH calculations, the F vs FeO^* and MgO trends of these Langmuir *et al.* calculations show only a subtle change in slope near cpx -out; the near linearity of the Langmuir *et al.* FeO^* and MgO trends reflects the model constraint that the Mg/Fe ratio of residual olivine and the Mg/Fe ratio of the bulk residue are equal. The offsets between the MELTS trends and the experimental data in the F – MgO and F – FeO^* space are, as for SiO_2 , the result of overstabilization of opx and understabilization of ol in the MELTS model (Hirschmann *et al.*, 1998b).

Figure 12e shows that the liquid compositions calculated with pMELTS, BATCH, and MELTS all parallel the F – CaO trend of the experimental DMM1 glasses, with BATCH matching most closely (as noted above, the Langmuir *et al.* model does not provide liquid CaO contents). Mean absolute deviations for the pMELTS and BATCH trends are 1.05 and 0.58 wt % CaO , respectively. With increasing melt fraction from the solidus up to cpx -out, the calculated liquid CaO contents increase gradually, as do the CaO concentrations in the experimental glasses. Above cpx -out, the CaO contents of the experimental glasses and all the calculated liquid compositions decrease rapidly with increasing F . Although BATCH reproduces the F vs CaO partial melting trend of DMM1, it is less successful in reproducing the low CaO contents in experimental glasses close to the fertile peridotite solidus; for example, using BATCH with MM3 as the starting composition, the calculated 10 kbar CaO content of the liquid at $F = 0.03$ is 2.3 wt % higher than the experimental glass (Baker & Stolper, 1994; Hirschmann *et al.*, 1998a; M. B. Baker, unpublished data, 1996). In contrast, for the same conditions, the pMELTS-calculated liquid is only 0.5 wt % low in CaO relative to the experimental results.

Although DMM1 was not included in the calibrations of either pMELTS or BATCH, both of these programs reproduce the essential characteristics of the melt fraction vs major element trends observed in the experimental glasses. The successes of these calculations include their generally close matches to the absolute values of the major oxide concentrations, their successful predictions of the overall shapes of the observed trends, their predictions of the changes in slope in the F vs SiO_2 , FeO^* , MgO , and CaO trends that occur at or near cpx -out, and their predictions of

cpx-out at values of F either within (pMELTS) or close to (BATCH) the experimental bracket. Nevertheless, liquid compositions calculated by all of the models display systematic offsets relative to the experimental glass compositions. Finally, although the Langmuir *et al.* model provides the best matches to the F vs FeO^* and MgO glass trends for DMM1, the absence of expressions for SiO_2 , Al_2O_3 , or CaO and the necessity of adjusting the subsolidus mode and melting reaction coefficient for *cpx* to optimize the calculated liquid compositions limit the usefulness of this approach.

Variations in solidus temperature as a function of peridotite bulk composition

McKenzie & Bickle (1988), Langmuir *et al.* (1992), Iwamori *et al.* (1995), Herzberg *et al.* (2000), and Hirschmann (2000) have compiled and parameterized available data on the solidi of fertile peridotite compositions in pressure–temperature space. The parameterizations of these studies are broadly consistent, and the rise in solidus temperature (T_s) with increasing pressure from 1 bar to 100 kbar is reasonably well constrained. The relationship between T_s and bulk composition at any given pressure, however, is less well quantified. Qualitatively, solidus temperature at constant pressure decreases in peridotites with increasing concentrations of incompatible elements (of which Na_2O , K_2O , and H_2O are likely to be the most important) and decreasing mg -number (Herzberg *et al.*, 2000; Hirschmann, 2000). Deconvolving the influence of these two compositional effects is generally difficult, as those peridotites with high alkali contents also tend to have relatively low mg -numbers. Linear fits of bulk peridotite $\text{Na}_2\text{O} + \text{K}_2\text{O}$ vs T_s and peridotite mg -number vs T_s by Herzberg *et al.* (2000) suggest that at 15 kbar, increasing the alkali content from 0.2 to 0.4 or decreasing the mg -number from 90 to 80 will produce a 30–35°C drop in T_s . However, mg -numbers and bulk alkali contents in the peridotite compositions fit by Herzberg *et al.* (2000) show an inverse correlation (correlation coefficient = 0.68), making it difficult to evaluate independently these two parameters.

Using an idealized ternary system as a framework for considering the effects of composition on solidus temperature, Hirschmann (2000) was able to model the negative correlation between solidus temperatures and incompatible element content (e.g. $\text{Na}_2\text{O} + \text{K}_2\text{O}$). His analysis, based on the cryoscopic expression (e.g. Carmichael *et al.*, 1974, pp. 170–173), showed that the bulk partition coefficients and concentrations of incompatible elements at the peridotite solidus are important parameters influencing the solidus temperature. In particular, the more incompatible an element, the larger its effect on the solidus (assuming melting is a

continuous reaction). He further showed that the conclusions drawn from the idealized ternary system could be applied to understanding variations in the solidus temperatures for MM3 (Baker & Stolper, 1994; Hirschmann *et al.*, 1998a; M. B. Baker, unpublished data, 1996), FER-B, FER-D, and FER-E (Pickering-Witter & Johnston, 2000) at 10 kbar, and MPy and Tinaquillo lherzolite (Robinson *et al.*, 1998) at 15 kbar.

We have extended the analysis of Hirschmann (2000) by considering eight peridotites for which the 10 kbar solidus has been determined and by including the effect of P_2O_5 in addition to Na_2O and K_2O . Because P_2O_5 contents in the bulk compositions of Pickering-Witter & Johnston (2000) and Schwab & Johnston (2001) are unknown, we have not included the solidus temperatures for these bulk compositions in our parameterization. The complete dataset includes DMM1 (this study), MM3 (Baker & Stolper, 1994; Hirschmann *et al.*, 1998a; M. B. Baker, unpublished data, 1996), syn-MM3 (Falloon *et al.*, 1999), KLB-1 and HK-66 (Takahashi & Kushiro, 1983; Hirose & Kushiro, 1993), HPy-40 (Jaques & Green, 1980), PHN1611 (Kushiro, 1996), and DW (Bertka & Holloway, 1994; this is a model Martian mantle composition). Bulk compositions are listed in Tables 1 and 5. These peridotites have solidus temperatures ranging from 1193 to 1272°C. Their concentrations of Na_2O , K_2O , and P_2O_5 are highly variable, ranging from 0.06 to 0.95, 0 to 0.22, and 0 to 0.16, and their mg -numbers range from 90.5 to 75.0. Experimentally determined solidus assemblages at 10 kbar include both spinel lherzolite and plagioclase + spinel lherzolite.

Most of these peridotites lack the necessary experimental data to estimate near-solidus liquid compositions. Thus, we have used pMELTS (Ghiorso *et al.*, 2002) to calculate 10 kbar near-solidus liquid compositions for these eight peridotites. The Na_2O , K_2O , and P_2O_5 contents of the pMELTS-calculated liquids at 10 kbar, QFM, and $F = 0.005$ range from 2.8 to 11.6, 0 to 11.3, and 0 to 8.6 wt %, respectively, and all of the calculated melts coexist with *ol*, *opx*, *cpx*, and *sp*. At $F = 0.005$, alkali feldspar is predicted to be a stable phase in the three peridotite compositions with the highest bulk alkali contents (PHN1611, HK-66, and HPy-40; these peridotites have bulk $\text{Na}_2\text{O} + \text{K}_2\text{O}$ contents of 0.47–1.17 wt %). pMELTS also predicts that whitlockite is stable at $F = 0.005$ in the five bulk compositions that have >0.017 wt % P_2O_5 (PHN1611, KLB-1, HPy-40, HK-66, and DW). It should be noted that, in this respect, results from pMELTS calculations differ from the expectations of the idealized ternary system analysis of Hirschmann (2000), in which it was assumed that the incompatible components never become a major structural constituent of a crystallizing phase and that the concentrations

Table 5: Bulk compositions used in modeling the 10 kbar peridotite solidus

	SiO ₂	TiO ₂	Al ₂ O ₃	Cr ₂ O ₃	FeO*	MnO	MgO	CaO	Na ₂ O	K ₂ O	P ₂ O ₅	NiO	mg-no. ¹
MM3 ²	45.5	0.11	3.98	0.68	7.18	0.13	38.3	3.57	0.31	0.008	0.004	0.23	90.48
syn-MM3 ³	45.5	0.11	3.98	0.68	7.18	0.13	38.3	3.57	0.31	0	0	0	90.48
KLB-1 ⁴	44.48	0.16	3.59	0.31	8.10	0.12	39.22	3.44	0.30	0.02	0.03	0.25	89.62
HK-66 ⁴	48.02	0.22	4.88	0.25	9.9	0.14	32.35	2.97	0.66	0.07	0.07	0.162	85.35
HPy-40 ⁵	47.9	1.18	5.91	0.72	8.81	0.13	28.8	5.14	0.95	0.22	0.06	0.13	85.35
PHN1611 ⁶	43.7	0.25	2.75	0.28	10.05	0.13	37.22	3.26	0.33	0.14	0.018	0.25	86.84
DW ⁷	44.4	0.14	3.02	0.75	17.9	0.46	30.2	2.45	0.5	0	0.16	0	75.05

¹mg-no. = 100MgO/(MgO + FeO*) on a molar basis with all Fe as FeO.

²MM3: Baker & Stolper (1994); bulk K₂O and P₂O₅ contents calculated from K₂O and P₂O₅ values in glasses from experiments on MM3 and mass balance constraints (Hirschmann *et al.*, 1998; M. B. Baker, unpublished data, 1996), mineral-liquid K₂O partition coefficients of Halliday *et al.* (1995), and ol-liq, opx-liq, and cpx-liq P₂O₅ partition coefficient values of 0.1, 0.03, and 0.05, respectively (Libourel *et al.*, 1994; Brunet & Chazot, 2001).

³Syn-MM3: target composition of Falloon *et al.* (1999); actual bulk composition not reported.

⁴KLB-1, HK-66: Hirose & Kushiro (1993); bulk NiO content of HK-66 calculated from NiO contents of olivine, spinel, orthopyroxene, and clinopyroxene and the proportions of these phases calculated by mass balance. NiO in orthopyroxene and clinopyroxene calculated using the reported olivine NiO concentration and mean opx-ol (0.26) and cpx-ol (0.13) NiO ratios in minerals from spinel lherzolites analyzed by Stosch (1981) and Hervig & Smith (1982).

⁵HPy-40: Jaques & Green (1980).

⁶PHN1611: Kushiro (1996); bulk NiO content from Morgan *et al.* (1980); bulk P₂O₅ content calculated from garnet P₂O₅ value (Smith *et al.*, 1993), mineral-garnet (gt) P₂O₅ partition coefficients measured in garnet lherzolites (ol-gt, 0.33; opx-gt, 0.11; cpx-gt, 0.78; Bishop *et al.*, 1978; Hervig & Smith, 1982), and the weight fractions of olivine, orthopyroxene, clinopyroxene, and garnet calculated by mass balance.

⁷DW: Bertka & Holloway (1994).

in near-solidus melts are controlled entirely by partitioning into the major peridotite phases.

Figure 13a shows that the experimentally determined solidus temperatures are well correlated with the concentrations of alkalis plus phosphorus in the calculated near-solidus melts. In addition to calculating liquid compositions at $F = 0.005$, we continued each pMELTS calculation down temperature and determined the model solidus for each peridotite ($T_{s,pMELTS}$). Figure 13b shows that the calculated $T_{s,pMELTS}$ values are correlated with the experimentally determined solidus temperatures, although the model temperatures are lower than the experimental determinations by $\sim 25\text{--}70^\circ\text{C}$ (the deviations are crudely correlated with the sum of the bulk alkali and phosphorus contents). The differences in temperature between the experimental and model solidi may reflect in part the difficulties in observing minute amounts of melt in experimental charges (each experimentally determined solidus temperature may be systematically too high), but they also probably reflect inaccuracies in the thermodynamic models that underpin pMELTS. The important point is that experimentally determined solidus temperatures are correlated with solidus temperatures and compositions of low-degree melts predicted by pMELTS, allowing us to utilize the thermodynamically consistent results of pMELTS as guides to the major factors controlling solidus temperature.

We have fitted the data shown in Fig. 13a to an equation of the form $T_s(^{\circ}\text{C}) = a_1 + a_2(\text{Na}_2\text{O}) + a_3(\text{K}_2\text{O}) + a_4(\text{P}_2\text{O}_5)$. The choice of this linear function is based on the simple case of solidus depression of a single phase by an incompatible element at infinite dilution (e.g. Hirschmann, 2000). That concept represents an oversimplification, and the presence of minor phases in the pMELTS calculations also complicates the application of this equation. The best fit ($a_1 = 1295.8$, $a_2 = -3.628$, $a_3 = -7.218$, $a_4 = -5.100$) reproduces the experimental solidus temperatures with a mean deviation of 3°C (less than half of the temperature uncertainty associated with any of the T_s determinations; Fig. 14). The largest temperature mismatch is for HK-66 (12°C), but the calculated T_s value is still within the experimental solidus bracket for this bulk composition (Fig. 14). Given the compositional complexities of natural peridotites, the simple functional form of the fit, and the difficulties in determining the solidus experimentally, the quality of the fit is actually somewhat surprising.

Although the peridotite bulk compositions span a range of mg-numbers (Tables 1 and 5), inclusion of an mg-number term in the equation does not improve the fit (i.e. the mean temperature deviation remains $\sim 3^\circ\text{C}$). It should be noted, however, that the model Martian mantle composition, DW, is the peridotite composition with the lowest mg-number, but it also

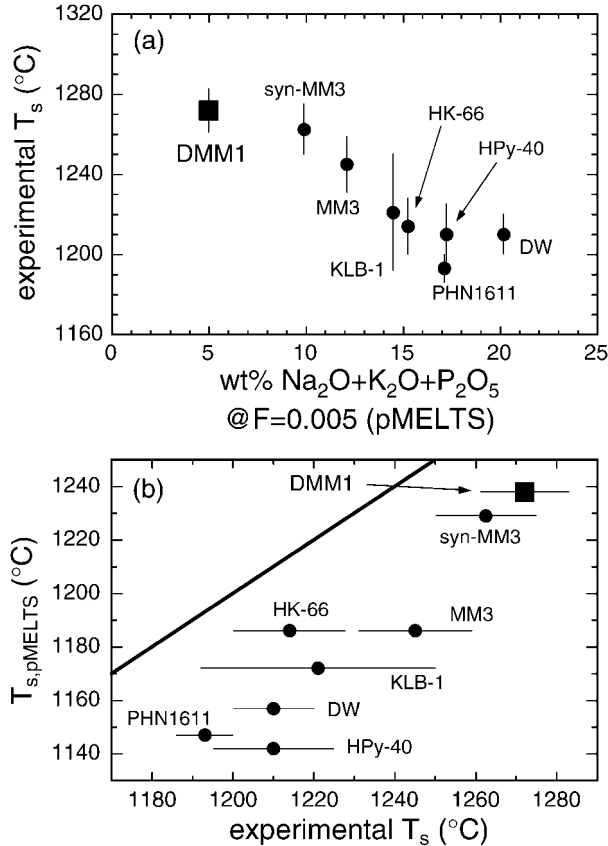


Fig. 13. (a) Experimentally determined solidus temperatures (T_s) for a range of peridotite bulk compositions plotted against wt % $\text{Na}_2\text{O} + \text{K}_2\text{O} + \text{P}_2\text{O}_5$ for near-solidus melts (0.5 wt %) calculated for the corresponding bulk compositions using pMELTS at 10 kbar and QFM. Bulk compositions are reported in Tables 1 and 5. Solidus temperatures and associated uncertainties were calculated from the experimental data in a variety of ways: (1) for DMM1 (this study, excluding run 23T) and MM3 (Baker & Stolper, 1994; Hirschmann *et al.*, 1998a; M. B. Baker, unpublished data, 1996) a weighted (using uncertainties on F and T) first- (DMM1) or second-order polynomial (MM3) of F vs T was computed using experiments saturated with the same set of major phases; uncertainties on T_s represent errors on the y -intercepts. (2) For some compositions, we digitized the P - T phase diagram or took the temperature midpoint between a subsolidus and a supersolidus experiment. For HK-66 (Takahashi & Kushiro, 1983), the uncertainty represents half the mean temperature differences for the 8 and 11 kbar subsolidus and supersolidus runs; for HPy-40 (Jaques & Green, 1980), we assigned an arbitrary uncertainty of $\pm 15^\circ\text{C}$; for syn-MM3 (Falloon *et al.*, 1999; a synthetic MM3 mix with no K_2O or P_2O_5); and for DW (Bertka & Holloway, 1994), uncertainties represent half the temperature difference between the lowest temperature supersolidus experiment and the highest temperature subsolidus run. (3) For the solidus, we took the midpoint between the lowest temperature 10 kbar run containing liquid and the temperature calculated by extrapolating the T vs F data (for $ol + opx + cpx \pm sp \pm plag$ -saturated melts) to $F = 0$ via an unweighted least-squares fit; uncertainties represent the difference between this midpoint temperature and the lowest temperature supersolidus run (KLB-1, Hirose & Kushiro, 1993; PHN1611, Kushiro, 1996). In both of these studies, the estimates of F reported for the low-temperature runs are too large because of an assumption that the bulk partition coefficient for either Na (Hirose & Kushiro, 1993) or K (Kushiro, 1996) is zero. The low-temperature 10 kbar runs of Hirose & Kushiro (1993) contain cpx and at the lowest temperature

has the highest P_2O_5 content and one of the highest Na_2O contents in our dataset. Thus, as stated above, mg -number and incompatible element concentrations tend to be correlated in peridotites, making it difficult to separate the effect of mg -number from those of alkalis. However, to evaluate the effect of mg -number on solidus temperature, we increased the mg -number of DMM1 (keeping the total number of moles of FeO and MgO constant) from 89.9 to 92 and used pMELTS to calculate the solidus temperature, which changed by only 2°C . This suggests that over the limited range of mg -numbers observed in the vast majority of spinel peridotite samples (~ 88 – 92 ; Herzberg *et al.*, 1988), mg -number will have no effect on T_s at 10 kbar.

In our parameterization, the coefficients for K_2O and P_2O_5 have similar absolute values that are larger than that for Na_2O . The larger effects on lowering of solidus temperature of the more incompatible components is precisely what was anticipated by Hirschmann (2000), suggesting that this simple fit has some validity as a predictive tool. Our expression for T_s suggests that the 10 kbar solidus temperature for an alkali- and phosphorus-free peridotite will be $\sim 1296^\circ\text{C}$. This is broadly consistent with the 1287 – 1289°C range for the 10 kbar solidus temperatures for the model peridotite compositions DF80 and JDS (with mg -numbers of 89.6 and 90.0, respectively) of Gudfinnsson & Presnall (2000) in CMASf based on mass balance constraints and their experimentally calibrated expressions for liquid and solid compositions in the plagioclase lherzolite field. Many abyssal peridotites have bulk compositions more strongly depleted in alkalis than DMM1 (Baker & Beckett, 1999; Fig. 1), and using our T_s expression and the abyssal peridotite compositions from Baker & Beckett (1999) that have the lowest and highest MgO contents, we predict that 10 kbar abyssal peridotite solidus temperatures would lie in the range of ~ 1278 – 1295°C .

CONCLUSIONS

(1) We conducted melting experiments on a depleted peridotite composition (DMM1) at 10 kbar using a modification of the diamond-aggregate melt-extraction technique in which diamonds were replaced by vitreous carbon spheres. Several approaches were used to demonstrate that melts segregated into

plagioclase. The lowest temperature run of Kushiro (1996) also contains plagioclase. (b) Comparison of 10 kbar experimental solidus temperatures (T_s , $^\circ\text{C}$) and the pMELTS-calculated solidus temperatures ($T_{s,pMELTS}$, $^\circ\text{C}$) for the eight peridotites listed in Tables 1 and 4. The pMELTS calculations were performed at 10 kbar and QFM. The temperature step in the pMELTS calculations was 1°C and the plotted point is the temperature at which $F = 0$. The diagonal continuous line is a 1:1 line shown for comparison.

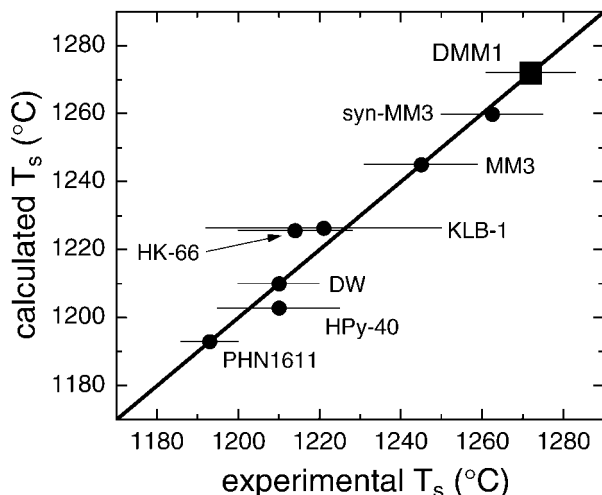


Fig. 14. Comparison of 10 kbar experimental solidus temperatures (T_s , °C) and solidus temperatures calculated using the expression in the text. The best-fit parameters used in the expression were solved for by minimizing the sum of the absolute deviations. The experimental solidus temperatures and their uncertainties are discussed in the caption to Fig. 13. The continuous diagonal 1:1 line is shown for comparison.

aggregates of vitreous carbon remained in chemical contact with the bulk charge over the course of the experiments down to melt fractions of ~ 0.02 – 0.04 and closely approached the compositions of equilibrium partial melts of the source composition.

(2) The most important differences between the compositions of partial melts of DMM1 and fertile peridotites at 10 kbar occur at low melt fractions. The differences in SiO_2 and CaO contents between low-degree melts of depleted and fertile peridotite are particularly striking. In contrast to results for fertile peridotites, SiO_2 contents of partial melts of DMM1 do not increase as melt fractions decrease from 0.1 to 0.02, resulting in differences of up to 6–8 wt % SiO_2 between partial melts of fertile and depleted lherzolites at 2% melting. Likewise, CaO contents of partial melts of depleted lherzolites are higher at *cpx*-out than partial melts of fertile lherzolites, and they decrease much less with decreasing melt fraction, resulting in 6–8 wt % more CaO in the partial melts of depleted lherzolites at 2% melting. Additionally, FeO^* and MgO contents do not decrease as dramatically in the partial melts of DMM1 as they do in partial melts of fertile peridotites over this range of melt fractions, and Na_2O contents are substantially lower in melts of DMM1. We infer that the substantially lower alkali contents in the near-solidus partial melts of DMM1 relative to those of fertile peridotite account for the differences in their SiO_2 , FeO^* , MgO, and CaO concentrations.

(3) The melting reaction for DMM1 at 10 kbar in the spinel lherzolite field is $0.57 \text{ opx} + 0.72 \text{ cpx} + 0.04 \text{ sp} = 0.35 \text{ ol} + 1 \text{ liq}$. The reaction coefficients are similar

to those determined for *ol* + *opx* + *cpx* + *sp*-saturated melting of fertile peridotite and analog mantle compositions in the $\text{CaO} + \text{MgO} + \text{Al}_2\text{O}_3 + \text{SiO}_2 + \text{FeO}$ system. In particular, *cpx* dominates the melting reaction over a wide range of peridotite compositions, and the *cpx* reaction coefficient is insensitive to the modal abundance of *cpx* in the lherzolite. Above *cpx*- and *sp*-out, DMM1 melts via the reaction $1.24 \text{ opx} = 0.24 \text{ ol} + 1 \text{ liq}$, which is also qualitatively similar to harzburgite melting reactions previously determined for fertile peridotites.

(4) pMELTS (Ghiorso *et al.*, 2002), BATCH (Longhi, 2002), and the expressions presented by Langmuir *et al.* (1992) were used to calculate partial melts of the DMM1 composition at 10 kbar. Although melts of depleted peridotites were not included in the calibrations of either pMELTS or BATCH, both of these programs reproduce the essential characteristics of the melt fraction vs major element trends observed in experiments on DMM1. The successes of these calculations include their generally close matches to the absolute values of the major oxide concentrations, their successful predictions of the overall shapes of the observed trends, their predictions of the changes in slope of the F vs SiO_2 , FeO^* , MgO, and CaO trends that occur at or near *cpx*-out, and their predictions of the melt fraction at which *cpx*-out occurs. Nevertheless, liquid compositions calculated by these models display systematic offsets relative to the experimental glass compositions. The Langmuir *et al.* expressions provide the best match to the F vs FeO^* and MgO glass trends for DMM1, but cannot be used to model SiO_2 , CaO, or Al_2O_3 contents of partial melts.

(5) Combining our experimentally determined solidus temperature with solidus temperatures determined on seven other peridotites, we parameterized T_s at 10 kbar as a function of the Na_2O , K_2O , and P_2O_5 contents in near-solidus liquids at $F = 0.005$ calculated with pMELTS. The resulting equation, $T_s(\text{°C}) = 1295.8 - (3.628)\text{Na}_2\text{O} - (7.218)\text{K}_2\text{O} - (5.100)\text{P}_2\text{O}_5$ (oxide quantities in wt %), recovers the input temperatures with a mean deviation of 3°C. This expression predicts that the 10 kbar solidi of abyssal peridotites are ~ 1278 – 1295 °C and is consistent with the theoretical expectation that more incompatible elements have a larger influence on the solidus.

ACKNOWLEDGEMENTS

The authors are grateful for helpful discussions with and/or laboratory support from Marc Hirschmann, Glenn Gaetani, John Beckett, and Paul Asimow. We thank Ian Hutcheon and Doug Phinney for assistance with the ion microprobe measurements. We also thank Charles Lesher, Keith Putirka, and Brandon Schwab

for helpful reviews. This work was supported by National Science Foundation grant OCE93-14505. This research was also funded in part by stipend support for L.E.W. from the National Physical Science Consortium and NASA-Johnson Space Center.

REFERENCES

- Albarède, F. & Provost, A. (1977). Petrological and geochemical mass-balance equations: an algorithm for least-square fitting and general error analysis. *Computers and Geosciences* **3**, 309–326.
- Allègre, C. J., Poirer, J.-P., Humler, E. & Hofmann, A. W. (1995). The chemical composition of the Earth. *Earth and Planetary Science Letters* **134**, 515–526.
- Armstrong, J. T. (1988). Quantitative analysis of silicate and oxide minerals, comparison of Monte Carlo, ZAF and $\phi(\rho z)$ procedures. In: Newbury, D. E. (ed.) *Microbeam Analysis*. San Francisco, CA: San Francisco Press, pp. 239–246.
- Asimow, P. D., Hirschmann, M. M. & Stolper, E. M. (1997). An analysis of variations in isentropic melt productivity. *Philosophical Transactions of the Royal Society of London, Series A* **355**, 255–281.
- Baker, M. B. & Beckett, J. R. (1999). The origin of abyssal peridotites, a reinterpretation of constraints based on primary bulk compositions. *Earth and Planetary Science Letters* **171**, 49–61.
- Baker, M. B. & Stolper, E. M. (1994). Determining the composition of high-pressure mantle melts using diamond aggregates. *Geochimica et Cosmochimica Acta* **58**, 2811–2827.
- Baker, M. B., Hirschmann, M. M., Ghiorso, M. S. & Stolper, E. M. (1995). Compositions of near-solidus peridotite melts from experiments and thermodynamic calculations. *Nature* **375**, 308–311.
- Baker, M. B., Hirschmann, M. M., Wasylenko, L. E., Stolper, E. M. & Ghiorso, M. S. (1996). Reply to, Quest for low degree mantle melts. *Nature* **381**, 286.
- Bertka, C. M. & Holloway, J. R. (1988). Martian mantle melts: an experimental study of iron-rich garnet lherzolite minimum melt composition. *Proceedings of the 18th Lunar and Planetary Science Conference*, 723–739.
- Bertka, C. M. & Holloway, J. R. (1994). Anhydrous partial melting of an iron-rich mantle. 1. Subsolidus phase assemblages and partial melting phase relations at 10 to 30 kbar. *Contributions to Mineralogy and Petrology* **115**, 313–322.
- Bishop, F. C., Smith, J. V. & Dawson, J. B. (1978). Na, K, P and Ti in garnet, pyroxene and olivine from peridotite and eclogite xenoliths from African kimberlites. *Lithos* **11**, 155–173.
- Brunet, F. & Chazot, G. (2001). Partitioning of phosphorus between olivine, clinopyroxene and silicate glass in a spinel lherzolite xenolith from Yemen. *Chemical Geology* **176**, 51–72.
- Cameron, M. & Papike, J. J. (1981). Structural and chemical variations in pyroxenes. *American Mineralogist* **66**, 1–50.
- Carmichael, I. S. E., Turner, F. J. & Verhoogen, J. (1974). *Igneous Petrology*. New York: McGraw-Hill.
- Christie, D. M., Carmichael, I. S. E. & Langmuir, C. H. (1986). Oxidation states of mid-ocean ridge basalt glasses. *Earth and Planetary Science Letters* **79**, 397–411.
- Daines, M. J. & Richter, F. M. (1988). An experimental method for directly determining the interconnectivity of melt in a partially molten system. *Geophysical Research Letters* **15**, 1459–1462.
- Dixon, J. E., Stolper, E. M. & Holloway, J. R. (1995). An experimental study of water and carbon-dioxide solubilities in mid-ocean ridge basaltic liquids. 1. Calibration and solubility models. *Journal of Petrology* **36**, 1607–1631.
- Dobson, P. F., Epstein, S. & Stolper, E. M. (1989). Hydrogen isotopic fractionation between coexisting vapor and silicate glasses and melts at low pressure. *Geochimica et Cosmochimica Acta* **53**, 2723–2730.
- Draper, D. S. & Green, T. H. (1999). *P–T* phase relations of silicic, alkaline, aluminous liquids: new results and applications to mantle melting and metasomatism. *Earth and Planetary Science Letters* **170**, 255–268.
- Falloon, T. J. & Green, D. H. (1987). Anhydrous partial melting of MORB pyroxene and other peridotite compositions at 10 kbar and implications for the origin of primitive MORB glasses. *Mineralogy and Petrology* **37**, 181–219.
- Falloon, T. J., Green, D. H., O'Neill, H. S. C. & Ballhaus, C. G. (1996). Quest for low degree mantle melts. *Nature* **381**, 285.
- Falloon, T. J., Green, D. H., O'Neill, H. S. C. & Hibberson, W. O. (1997). Experimental tests of low degree peridotite partial melt compositions, implications for the nature of anhydrous near-solidus peridotite melts at 1 GPa. *Earth and Planetary Science Letters* **152**, 149–162.
- Falloon, T. J., Green, D. H., Danyushevsky, L. V. & Faul, U. H. (1999). Peridotite melting at 1.0 and 1.5 GPa, an experimental evaluation of techniques using diamond aggregates and mineral mixes for determination of near-solidus melts. *Journal of Petrology* **40**, 1343–1375.
- Falloon, T. J., Danyushevsky, L. V. & Green, D. H. (2001). Peridotite melting at 1 GPa: reversal experiments on partial melt compositions produced by peridotite–basalt sandwich experiments. *Journal of Petrology* **42**, 2363–2390.
- Gaetani, G. A. & Grove, T. L. (1998). The influence of water on melting of mantle peridotite. *Contributions to Mineralogy and Petrology* **131**, 323–346.
- Gee, L. L. & Sack, R. O. (1988). Experimental petrology of melilite nephelinites. *Journal of Petrology* **24**, 256–265.
- Ghiorso, M. S. & Sack, R. O. (1995). Chemical mass-transfer in magmatic processes 4. A revised and internally consistent thermodynamic model for the interpolation and extrapolation of liquid–solid equilibria in magmatic systems at elevated temperatures and pressures. *Contributions to Mineralogy and Petrology* **119**, 197–212.
- Ghiorso, M. S., Hirschmann, M. M., Reiners, P. W. & Kress, V. C. (2002). The pMELTS: a revision of MELTS for improved calculation of phase relations and major element partitioning related to partial melting of the mantle to 3 GPa. *Geochemistry, Geophysics, Geosystems* **3** (Paper 2001GC000217).
- Green, D. H., Falloon, T. J. & Taylor, W. R. (1987). Mantle derived magmas, role of variable source peridotite and variable C–H–O fluid compositions. In: Mysen, B. O. (ed.) *Magmatic Processes, Physicochemical Principles*. University Park, PA: United States Geochemical Society, pp. 139–154.
- Gudfinnsson, G. & Holloway, J. R. (1993). Activity–composition relationships in the system Fe–Pt at 1300 and 1400°C and at 1 atm and 20 kbar. *American Mineralogist* **78**, 178–186.
- Gudfinnsson, G. & Presnall, D. C. (2000). Melting behavior of model lherzolite in the system CaO–MgO–Al₂O₃–FeO at 0.7–2.8 GPa. *Journal of Petrology* **41**, 1241–1269.
- Gudfinnsson, G., Holloway, J. R. & Carmichael, I. S. E. (1988). Pressure effect on the ferric/ferrous ratio in basaltic liquids. *EOS Transactions, American Geophysical Union* **69**, 1511.
- Halliday, A. N., Lee, D.-C., Tommasini, S., Davies, G. R., Paslick, C. R., Fitton, J. G. & James, D. E. (1995). Incompatible trace elements in OIB and MORB and source enrichment in the sub-oceanic mantle. *Earth and Planetary Science Letters* **133**, 379–395.
- Hart, S. R. & Zindler, A. (1986). In search of a bulk-earth composition. *Chemical Geology* **57**, 247–267.

- Hays, J. F. (1966). Lime–alumina–silica. *Carnegie Institute of Washington Yearbook* **65**, 234–239.
- Hellebrand, E., Snow, J. E., Dick, H. J. B. & Hofmann, A. W. (2000). Coupled major and trace elements as indicators of the extent of melting in mid-ocean-ridge peridotites. *Nature* **410**, 677–681.
- Hervig, R. L. & Smith, J. V. (1982). Temperature-dependent distribution of Cr between olivine and pyroxenes in lherzolite xenoliths. *Contributions to Mineralogy and Petrology* **81**, 184–189.
- Herzberg, C. T., Feigenson, M., Skuba, C. & Ohtani, E. (1988). Majorite fractionation recorded in the geochemistry of peridotites from South Africa. *Nature* **332**, 823–826.
- Herzberg, C. T., Ratteron, P. & Zhang, J. (2000). New experimental observations on the anhydrous solidus for peridotite KLB-1. *Geochemistry, Geophysics, Geosystems* **1** (Paper 2000GC000089).
- Hirose, K. & Kushiro, I. (1993). Partial melting of dry peridotites at high pressures: determination of compositions of melts segregated from peridotite using aggregates of diamond. *Earth and Planetary Science Letters* **114**, 477–489.
- Hirschmann, M. M. (2000). Mantle solidus, experimental constraints and the effects of peridotite composition. *Geochemistry, Geophysics, Geosystems* **1** (Paper 2000GC000070).
- Hirschmann, M. M., Baker, M. B. & Stolper, E. M. (1998a). The effect of alkalis on the silica content of mantle-derived melts. *Geochimica et Cosmochimica Acta* **62**, 883–902.
- Hirschmann, M. M., Ghiorso, M. S., Wasylenko, L. E., Asimow, P. D. & Stolper, E. M. (1998b). Calculation of peridotite partial melting from thermodynamic models of minerals and melts. I. Review of methods and comparison with experiments. *Journal of Petrology* **39**, 1091–1115.
- Hirschmann, M. M., Ghiorso, M. S. & Stolper, E. M. (1999a). Calculation of peridotite partial melting from thermodynamic models of minerals and melts. II. Isobaric variations in melts near the solidus and owing to variable source composition. *Journal of Petrology* **40**, 297–313.
- Hirschmann, M. M., Asimow, P. D., Ghiorso, M. S. & Stolper, E. M. (1999b). Calculation of peridotite partial melting from thermodynamic models of minerals and melts. III. Controls on isobaric melt production and the effect of water on melt production. *Journal of Petrology* **40**, 831–851.
- Huebner, J. S. (1971). Buffering techniques for hydrostatic systems at elevated pressures. In: Ulmer, G. C. (ed.) *Research Techniques for High Pressure and High Temperature*. New York: Springer, pp. 123–177.
- Ihinger, P. D., Zhang, Y. & Stolper, E. M. (1999). The speciation of dissolved water in rhyolitic melt. *Geochimica et Cosmochimica Acta* **63**, 3567–3578.
- Iwamori, H., McKenzie, D. & Takahashi, E. (1995). Melt generation by isentropic mantle upwelling. *Earth and Planetary Science Letters* **134**, 253–266.
- Jamieson, H. E., Roeder, P. L. & Grant, A. H. (1992). Olivine–pyroxene–PtFe alloy as an oxygen geobarometer. *Journal of Geology* **100**, 138–145.
- Jaques, A. L. & Green, D. H. (1980). Anhydrous melting of peridotite at 0–15 kb pressure and the genesis of tholeiitic basalts. *Contributions to Mineralogy and Petrology* **73**, 287–310.
- Jarosewich, E., Nelen, J. A. & Norberg, J. A. (1979). Electron microprobe reference samples for mineral analysis. *Smithsonian Contributions to Earth Sciences* **22**, 68–72.
- Johnson, K. T. M. & Dick, H. J. B. (1992). Open system melting and temporal and spatial variation of peridotite and basalt in the Atlantis Fracture Zone. *Journal of Geophysical Research* **97**, 9219–9241.
- Johnson, K. T. M. & Kushiro, I. (1992). Segregation of high-pressure partial melts from peridotite using aggregates of diamonds: a new experimental approach. *Geophysical Research Letters* **19**, 1703–1706.
- Johnson, K. T. M., Dick, H. J. B. & Shimizu, N. (1990). Melting in the oceanic upper mantle: an ion microprobe study of diopsides in abyssal peridotites. *Journal of Geophysical Research* **95**, 2661–2678.
- Kent, A. J. R., Norman, M. D., Hutcheon, I. D. & Stolper, E. M. (1999). Seawater assimilation in an oceanic volcano: evidence from matrix glasses and glass inclusions from Loihi seamount, Hawaii. *Chemical Geology* **156**, 299–319.
- Kinzler, R. J. (1997). Melting of mantle peridotite at pressures approaching the spinel to garnet transition: application to mid-ocean ridge basalt petrogenesis. *Journal of Geophysical Research* **102**, 853–874.
- Kinzler, R. J. & Grove, T. L. (1992a). Primary magmas of mid-ocean ridge basalts 1. Experiments and methods. *Journal of Geophysical Research* **97**, 6885–6906.
- Kinzler, R. J. & Grove, T. L. (1992b). Primary magmas of mid-ocean ridge basalts 2. Applications. *Journal of Geophysical Research* **97**, 6907–6926.
- Kushiro, I. (1975). On the nature of silicate melt and its significance in magma genesis, regularities in the shift of the liquidus boundaries involving olivine, pyroxene, and silica minerals. *American Journal of Science* **275**, 411–431.
- Kushiro, I. (1996). Partial melting of a fertile mantle peridotite at high pressures, an experimental study using aggregates of diamond. In: Basu, A. & Hart, S. (eds) *Earth Processes, Reading the Isotopic Code*. American Geophysical Union Monograph **95**, 109–122.
- Kushiro, I. & Mysen, B. O. (2002). A possible effect of melt structure on the Mg–Fe²⁺ partitioning between olivine and melt. *Geochimica et Cosmochimica Acta* **66**, 2267–2272.
- Langmuir, C. H., Klein, E. M. & Plank, T. (1992). Petrological systematics of mid-ocean ridge basalts, constraints on melt generation beneath ocean ridges. In: Morgan, J. P., Blackman, D. & Sinton, J. (eds) *Mantle Flow and Melt Generation at Mid-Ocean Ridges*. American Geophysical Union Monograph **71**, 183–280.
- Leshner, C. E. & Walker, D. (1988). Cumulate maturation and melt migration in a temperature gradient. *Journal of Geophysical Research* **93**, 10295–10311.
- Libourel, G., Deloule, E. & Toplis, M. J. (1994). Phosphorus partitioning in basalts: an experimental and ion probe study. *Mineralogical Magazine* **58A**, 527–528.
- Longhi, J. (2002). Some phase equilibria systematics of lherzolite melting. *Geochemistry, Geophysics, Geosystems* **3**, U1–U33.
- Mattioli, G. S. & Wood, B. J. (1988). Magnetite activities across the Mg₂AlO₄–Fe₃O₄ spinel join, with application to thermobarometric estimates of upper mantle oxygen fugacity. *Contributions to Mineralogy and Petrology* **98**, 148–162.
- Mattioli, G. S., Baker, M. B., Rutter, M. J. & Stolper, E. M. (1989). Upper mantle oxygen fugacity and its relationship to metasomatism. *Journal of Geology* **97**, 521–536.
- McDonough, W. F. & Sun, S.-S. (1995). The composition of the Earth. *Chemical Geology* **120**, 223–253.
- McKenzie, D. (1984). The generation and compaction of partially molten rock. *Journal of Petrology* **25**, 713–765.
- McKenzie, D. (1985). The extraction of magma from the crust and mantle. *Earth and Planetary Science Letters* **74**, 81–91.
- McKenzie, D. (1989). Some remarks on the movement of small melt fractions in the mantle. *Earth and Planetary Science Letters* **95**, 53–72.

- McKenzie, D. & Bickle, M. J. (1988). The volume and composition of melt generated by extension of the lithosphere. *Journal of Petrology* **29**, 625–679.
- Morgan, J. W., Wandler, G. A. & Petrie, R. K. (1980). Earth's upper mantle: volatile element distribution and origin of siderophile element content. *Lunar and Planetary Science* **XI**, 740–742.
- Niu, Y. & Batiza, R. (1991). An empirical method for calculating melt compositions produced beneath mid-ocean ridges: application to axis and off-axis (seamounts) melting. *Journal of Geophysical Research* **96**, 21753–21777.
- Niu, Y. & Hékinian, R. (1997). Spreading rate dependence of the extent of mantle melting beneath ocean ridges. *Nature* **385**, 326–329.
- Noda, T., Inagaki, M. & Yamada, S. (1969). Glass-like carbons. *Journal of Non-Crystalline Solids* **1**, 285–302.
- O'Neill, H. S. C. & Wall, V. J. (1987). The olivine–orthopyroxene–spinel oxygen geobarometer, the nickel precipitation curve, and the oxygen fugacity of the Earth's upper mantle. *Journal of Petrology* **28**, 1169–1191.
- Pickering-Witter, J. & Johnston, A. D. (2000). The effects of variable bulk composition on the melting systematics of fertile peridotitic assemblages. *Contributions to Mineralogy and Petrology* **140**, 190–211.
- Reed, B. C. (1992). Linear least-squares fits with errors in both coordinates. II: Comments on parameter variances. *American Journal of Physics* **60**, 59–62.
- Ringwood, A. E. (1979). *Origin of the Earth and Moon*. New York: Springer.
- Robinson, J. A. C., Wood, B. J. & Blundy, J. D. (1998). The beginning of melting of fertile and depleted peridotite at 1.5 GPa. *Earth and Planetary Science Letters* **155**, 97–111.
- Ryerson, F. J. (1985). Oxide solution mechanisms in silicate melts—systematic variations in the activity-coefficient of SiO₂. *Geochimica et Cosmochimica Acta* **49**, 637–649.
- Sack, R. O., Carmichael, I. S. E., Rivers, M. L. & Ghiorsio, M. S. (1980). Ferric–ferrous equilibria in natural silicate liquids at 1 bar. *Contributions to Mineralogy and Petrology* **75**, 369–376.
- Salters, V. J. M. & Dick, H. J. B. (2002). Mineralogy of the mid-ocean-ridge basalt source from neodymium isotopic composition of abyssal peridotites. *Nature* **418**, 68–72.
- Sawa, T. & Tanaka, K. (2002). Nanoindentation of natural diamond. *Philosophical Magazine A—Physics of Condensed Matter: Structure, Defects, and Mechanical Properties* **82**, 1851–1856.
- Schwab, B. E. & Johnston, A. D. (2001). Melting systematics of modally variable, compositionally intermediate peridotites and the effect of mineral fertility. *Journal of Petrology* **42**, 1789–1811.
- Sen, G. (1982). Composition of basaltic liquids generated from a partially depleted lherzolite at 9 kbar pressure. *Nature* **299**, 336–338.
- Shimizu, N. (1998). The geochemistry of olivine-hosted melt inclusions in a FAMOUS basalt ALV19-4-1. *Physics of the Earth and Planetary Interiors* **107**, 183–201.
- Smith, D., Griffin, W. L. & Ryan, C. G. (1993). Compositional evolution of high-temperature sheared lherzolite PHN 1611. *Geochimica et Cosmochimica Acta* **57**, 605–613.
- Sobolev, A. V. (1996). Melt inclusions in minerals as a source of principle petrological information. *Petrology* **4**, 209–220.
- Sobolev, A. V. & Shimizu, N. (1993). Ultra-depleted primary melt included in an olivine from the Mid-Atlantic Ridge. *Nature* **363**, 151–154.
- Stevenson, D. J. & Scott, D. R. (1991). Mechanics of fluid–rock systems. *Annual Review of Fluid Mechanics* **23**, 305–339.
- Stineman, R. W. (1980). A consistently well-behaved method of interpolation. *Creative Computing* **6**, 54–57.
- Stolper, E. M. & Newman, S. (1994). The role of water in the petrogenesis of Mariana trough magmas. *Earth and Planetary Science Letters* **121**, 293–325.
- Stosch, H.-G. (1981). Sc, Cr, Co and Ni partitioning between minerals from spinel peridotite xenoliths. *Contributions to Mineralogy and Petrology* **78**, 166–174.
- Sun, S.-S. (1982). Chemical composition and origin of the earth's primitive mantle. *Geochimica et Cosmochimica Acta* **46**, 179–192.
- Takahashi, E. (1986). Melting of a dry peridotite KLB-1 up to 14 GPa, implications on the origin of peridotitic upper mantle. *Journal of Geophysical Research* **91**(B8), 9367–9380.
- Takahashi, E. & Kushiro, I. (1983). Melting of a dry peridotite at high pressures and basalt magma genesis. *American Mineralogist* **68**, 859–879.
- Ulmer, P. (1989). The dependence of the Fe²⁺–Mg cation partitioning between olivine and basaltic liquid on pressure, temperature and composition, an experimental study to 30 kbars. *Contributions to Mineralogy and Petrology* **101**, 261–273.
- von Bargen, N. & Waff, H. S. (1986). Permeabilities, interfacial areas and curvatures of partially molten systems, results of numerical computations of equilibrium microstructures. *Journal of Geophysical Research* **91**, 9261–9276.
- Waff, H. S. & Bulau, J. R. (1979). Equilibrium fluid distribution in an ultramafic partial melt under hydrostatic stress conditions. *Journal of Geophysical Research* **84**, 6109–6114.
- Wagner, T. P. & Grove, T. L. (1998). Melt/harzburgite reaction in the petrogenesis of tholeiitic magma from Kilauea volcano, Hawaii. *Contributions to Mineralogy and Petrology* **131**, 1–12.
- Walter, M. J. (1998). Melting of garnet peridotite and the origin of komatiite and depleted lithosphere. *Journal of Petrology* **39**, 29–60.
- Wänke, H., Dreibus, G. & Jagoutz, E. (1984). Mantle chemistry and accretion history of the earth. In: Kröner, A., Hanson, G. & Goodwin, A. (eds) *Archean Geochemistry*. Berlin: Springer, pp. 1–24.
- Wasylenko, L. E., Baker, M. B., Hirschmann, M. M. & Stolper, E. M. (1996). The effect of source depletion on equilibrium mantle melting. *EOS Transactions, American Geophysical Union* **77**(46), F847.